2000

Studies of the inclusive semileptonic decays of the b-hadrons

Jong Il Yi
Iowa State University

INFORMATION TO USERS

This manuscript has been reproduced from the microfilm master. UMI films the text directly from the original or copy submitted. Thus, some thesis and dissertation copies are in typewriter face, while others may be from any type of computer printer.

The quality of this reproduction is dependent upon the quality of the copy submitted. Broken or indistinct print, colored or poor quality illustrations and photographs, print bleedthrough, substandard margins, and improper alignment can adversely affect reproduction.

In the unlikely event that the author did not send UMI a complete manuscript and there are missing pages, these will be noted. Also, if unauthorized copyright material had to be removed, a note will indicate the deletion.

Oversize materials (e.g., maps, drawings, charts) are reproduced by sectioning the original, beginning at the upper left-hand corner and continuing from left to right in equal sections with small overlaps.

Photographs included in the original manuscript have been reproduced xerographically in this copy. Higher quality 6" x 9" black and white photographic prints are available for any photographs or illustrations appearing in this copy for an additional charge. Contact UMI directly to order.

Bell & Howell Information and Learning
300 North Zeeb Road, Ann Arbor, MI 48106-1346 USA
800-521-0600

Studies of the inclusive semileptonic decays of the *b*-hadrons

by

Jong Il Yi

A dissertation submitted to the graduate faculty

in partial fulfillment of the requirements for the degree of

DOCTOR OF PHILOSOPHY

Major: High Energy Physics

Major Professor: Eli Rosenberg

Iowa State University

Ames, Iowa

2000

UMI Number: 9990504

Bell & Howell Information and Learning Company
300 North Zeeb Road
P.O. Box 1346
Ann Arbor, MI 48106-1346

Graduate College
Iowa State University

This is to certify that the doctoral dissertation of

Jong Il Yi

has met the dissertation requirements of Iowa State University

Signature was redacted for privacy.

Committee Member

Signature was redacted for privacy.

Committee Member

Signature was redacted for privacy.

Committee Member

Signature was redacted for privacy.

Committee Member

Signature was redacted for privacy.

Major Professor

Signature was redacted for privacy.

For the Major Program

Signature was redacted for privacy.

For the Graduate College

To My Parents

TABLE OF CONTENTS

ABSTRACT xi

1 INTRODUCTION 1

1.1 Motivation and history 3

1.2 Current status 5

1.3 Strategy 6

1.4 Outline 11

2 THEORETICAL POINT OF VIEW 12

2.1 The basics and the dilemma 14

2.2 Any ideas? 18

2.3 Leptonic energy spectrum 19

2.3.1 Inclusive approach 19

2.3.2 Exclusive approach 20

3 HARDWARE AND PERFORMANCE 24

3.1 The LEP collider 24

3.2 The DELPHI detector 29

3.2.1 Event topology 29

3.2.2 Reconstructing tracks 32

3.2.3 Particle identification 36

3.2.4 Detection of electrons 40

3.2.5 Detection of muons 44

3.2.6 Triggering and data acquisition 46

4 PREPARATION 49

4.1 Event selection 49

4.1.1 Preselection 50

4.1.2 Enhancing b-quark events 51

4.2 b-hadron charge determination 53

4.2.1 Reconstruction of b-hadrons 55

4.2.2 Charge determination 56

4.3 Simulation data 64

4.3.1 Simulation 64

4.3.2 Leptonic spectra 66

4.3.3 Simulated leptons versus real leptons 67

4.3.4 Upper–vertex simulation 70

5 RESULTS 72

5.1 Lepton spectra and background 73

5.2 Fitting and results 75

5.3 Systematics uncertainties 76

5.3.1 Experimental uncertainties 79

5.3.2 Theoretical uncertainties 83

5.4 Summary of results 87

6 CONCLUSION 89

6.1 Summary of DELPHI results 90

6.2 Concluding remarks 93

REFERENCES 95

ACKNOWLEDGMENTS 98

LIST OF TABLES

Table 1.1 Three generations of quarks and leptons 2

Table 1.2 Force mediators (bosons) 2

Table 1.3 Published measurements of semileptonic branching fraction by various experiments 5

Table 1.4 Newer measurements of $\mathcal{B}_{SL}$ from the LEP experiments 8

Table 4.1 Initial selection results 52

Table 4.2 Input parameters for b-purity calculation 53

Table 4.3 Number of simulated events 66

Table 4.4 Parameters for $b \to c \to \ell$ models 67

Table 4.5 Applied ratios of efficiencies and misidentification probabilities to simulated leptons 68

Table 5.1 Fitting results with statistical uncertainties 76

Table 5.2 Correlation matrix in the fitting 79

Table 5.3 Summary of results from the fitting procedure 79

Table 5.4 Uncertainties from correlation studies 80

Table 5.5 Uncertainties resulting from lepton treatment 82

Table 5.6 Uncertainties resulting from b-tagging procedure 83

Table 5.7 Uncertainties in fitting with finite simulation sample 83

Table 5.8 Uncertainties in the choice of fragmentation model 84

Table 5.9 Uncertainties from the assumed branching fractions 86

Table 5.10 Uncertainties resulting from the dependency of decay models 87

Table 5.11 Combined systematic uncertainties 88

LIST OF FIGURES

Figure 1.1 Theoretical bounds for $\mathcal{B}_{SL}$ and n_c 7

Figure 1.2 Charge correlation method 9

Figure 1.3 Same-sign leptons in the upper–vertex decay 10

Figure 1.4 Expected momentum spectra for same–sign and opposite–sign leptons 10

Figure 2.1 Decay of a b-hadron in the spectator model 13

Figure 2.2 Comparison among the different theoretical models 23

Figure 2.3 Contributions to $\mathcal{B}_{SL}$ under ISGW model 23

Figure 3.1 The DELPHI detector 25

Figure 3.2 Particle acceleration procedure 27

Figure 3.3 Contribution to the total cross section in the process of $e^+e^- \rightarrow \gamma, Z^0 \rightarrow$ anything 28

Figure 3.4 Three-dimensional view of a hadronic event 31

Figure 3.5 A simple representation of a b event 31

Figure 3.6 Three concentric layers of microvertex detector 34

Figure 3.7 TPC is shown with a charged particle passing through. 35

Figure 3.8 Specific energy loss dE/dx in the TPC as a function of particle momentum 38

Figure 3.9 Average Čerenkov angle per track as a function of momentum in RICH 39

Figure 3.10 Separation between kaons and other particles 40
Figure 3.11 Fractional electron energy loss per radiation length 41
Figure 3.12 Simplified illustration of electromagnetic cascades 42
Figure 3.13 Schematic view of an HPC module 43
Figure 3.14 Arrangement of muon chambers 45

Figure 4.1 Efficiency versus purity is shown for the b-tagging technique. 54
Figure 4.2 Rapidity distribution 56
Figure 4.3 Reconstructed b-hadron energy 57
Figure 4.4 A schematic view of a neural network 59
Figure 4.5 Input variables used in neural network to separate b decay products from fragmentation particles 61
Figure 4.6 Separation between fragmentation and b tracks 62
Figure 4.7 Estimated charge of b-hadron 63
Figure 4.8 Separation between b and $\bar{b}$ hadrons 65
Figure 4.9 Semileptonic momentum spectra for different models 68
Figure 4.10 Secondary lepton momentum spectra for different models . . 69
Figure 4.11 Upper–vertex lepton spectrum 71

Figure 5.1 Resolution of k^* 74
Figure 5.2 Fitting results for the $b \to c \to \ell$ models 77
Figure 5.3 Fitting results for the $b \to \ell$ models 78
Figure 5.4 Results of fitting the lepton spectrum without the charge correlation. 81
Figure 5.5 Fragmentation functions for different quarks 85
Figure 5.6 Shapes of the upper–vertex lepton spectrum 86

Figure 6.1 Measured $\mathcal{B}_{SL}$ shown with theoretical boundary 92

Figure 6.2 CLEO analysis 94

ABSTRACT

A detailed description of a new analysis, in which the correlation of the electric charge of the b-quark to that of the lepton is utilized to isolate different decay modes of the b-hadrons, is presented. Using the data collected by the DELPHI detector during the 1994 and 1995 data-taking periods, the inclusive b-hadron semileptonic branching fraction is measured to be

$$\mathrm{BR}(b \to \ell)(\%) = 10.75 \pm 0.15(\mathrm{stat}) \pm 0.28(\mathrm{syst})^{-0.24}_{-0.43}(\mathrm{model}).$$

Along with the semileptonic branching fraction, the branching fractions for the cascade mode, $b \to c \to \ell$, and the upper–vertex mode, $b \to \bar{c} \to \ell$, are also measured:

$$\mathrm{BR}(b \to c \to \ell)(\%) = 7.99 \pm 0.27(\mathrm{stat}) \pm 0.28(\mathrm{syst})^{-0.21}_{-0.10}(\mathrm{model})$$

$$\mathrm{BR}(b \to \bar{c} \to \ell)(\%) = 1.34 \pm 0.30(\mathrm{stat}) \pm 0.29(\mathrm{syst})^{-0.36}_{-0.58}(\mathrm{model}).$$

1 INTRODUCTION

Baffling: a word such as that represents a piece of humanity, as it fuels the mind to question the unknown and to understand the fundamentals. It is in this spirit that we have reached our current understanding of the universe in which we live. This understanding is delicately expressed in a collection of theories known as the Standard Model of the elementary particles. In this model, the fundamental particles are described in terms of their interactions. These interactions represent three of the nature's four fundamental forces: strong, weak and electromagnetic. The fourth fundamental force, gravity, is yet to be included in the model and continues to be the fuel behind the drive to improve our understanding.

The Standard Model contains six quarks, six leptons and their anti-partners as the fundamental particles and the mediators of different types of force as shown in Tables 1.1 and 1.2. The quarks and leptons are spin-$\frac{1}{2}$ particles and are, therefore, called fermions. While the leptons can be observed as free particles, the quarks have not been. The bound state in which the quarks are confined is called a hadron. There are two types of hadrons: a meson containing a quark and an anti-quark, $q_1\bar{q}_2$, and a baryon containing three quarks, $q_1q_2q_3$. The interactions among the particles take place by exchanging an appropriate force mediator, a boson. The existence of these particles and the interactions described within the Standard Model have all been confirmed.

The worthiness of a theory, however, lies not only on the ability to explain the observed phenomena but also in the power to predict. The Standard Model has been

Table 1.1 Three generations of quarks and leptons

	name	symbol	approximate mass[a]	charge
quarks	up	u	$0.004\ GeV/c^2$	$+\frac{2}{3}e$
	down	d	$0.007\ GeV/c^2$	$-\frac{1}{3}e$
	charm	c	$1.3\ GeV/c^2$	$+\frac{2}{3}e$
	strange	s	$0.3\ GeV/c^2$	$-\frac{1}{3}e$
	top	t	$180\ GeV/c^2$	$+\frac{2}{3}e$
	bottom	b	$4.8\ GeV/c^2$	$-\frac{1}{3}e$
leptons	electron	e	$0.0005\ GeV/c^2$	$-e$
	e-neutrino	ν_e	≈ 0	0
	muon	μ	$0.106\ GeV/c^2$	$-e$
	μ-neutrino	ν_e	≈ 0	0
	tau	τ	$1.777\ GeV/c^2$	$-e$
	τ-neutrino	ν_e	≈ 0	0

[a] Since quarks are found only in bound states, the definition of a quark mass is ambiguous. Listed are the "free" quark masses.

Table 1.2 Force mediators (bosons)

name	Symbol	approximate mass	Force
gluon	g	0	Strong
W	$W^{\pm}$	$81\ GeV/c^2$	Weak
Z	Z^0	$92\ GeV/c^2$	Weak
photon	γ	0	Electromagnetic

successful in that it explains many experimental results and predicts many more. However, a theory is not a fact; it serves as a guideline until enough discrepancies lead to a more robust theory. This thesis presents a test of our theory. In it, a possible discrepancy is proposed. To validate the proposal, the accuracy of and the confidence in the experimental measurement are questioned. Efforts are made by a number of groups in both theoretical and experimental sides to counter the proposal. In what follows, one effort in the experimental side to test the validity of the proposal is presented.

1.1 Motivation and history

In a published paper in 1994, a group of physicists declared one particular quantity, calculated from the Standard Model, baffling [1]. The quantity, is what is called the semileptonic branching fraction of the b-hadron. When a hadron containing a b-quark, a b-hadron, decays into final states containing a lepton pair and lighter hadrons, the b-hadron is said to have decayed semileptonically. The fraction in which this takes place is known as the semileptonic branching fraction.

The semileptonic decay has its roots in the nuclear β-decay, where a lepton pair, an electron and its neutrino, is released in a decay of a neutron into a proton, or more precisely, in a decay of a d-quark into a u-quark. This decay, which opened the door to the physics of weak interaction, serves as an important tool to study one of the fundamental questions of quark generation. The question has to do with how the carrier of weak interaction, W, couples to quarks. When leptons are coupled with W, $W \rightarrow \ell^- \nu_\ell$, the strength of the coupling is the same for all three generations of leptons. It is also observed that the transition from a lepton of one generation to a lepton of another does not take place. In contrast to the lepton case, when quarks are coupled with W, $W \rightarrow q_1 q_2$, the strength of the coupling depends on which quarks are coupled and is proportional to $V_{q_1 q_2}$. In addition, the transition between a quark of one generation and a quark of another is possible, an example of which can be seen in the semileptonic decay of a b-quark: $b \rightarrow W^{*-} c$, $W^{*-} \rightarrow \ell^- \bar{\nu}$, where W^* is a virtual W[1]. The strengths of all the possible transitions among quarks can then be expressed in a matrix:

$$V_{q_1 q_2} = \begin{pmatrix} V_{ud} & V_{us} & V_{ub} \\ V_{cd} & V_{cs} & V_{cb} \\ V_{td} & V_{ts} & V_{tb} \end{pmatrix}.$$

[1]From this point on, virtual W is implied for every occurrence of W in the decay of a b-quark, since b-quark mass is insufficient to create a real W.

This matrix is known as the Cabibbo-Kobayashi-Maskawa (CKM) matrix. The elements of CKM matrix must be measured, and most of the known elements have been determined from semileptonic decays. The diagonal elements are close to unity, and the elements farther away from the diagonal are smaller in magnitude. The existence and the structure of CKM matrix have been implicated as the source of charge–parity (CP) violation, combined violation of particle–antiparticle conjugation and parity reversal of coordinate system. As CP violation is one of the fundamental properties of physics, the question of whether or not this implication is true goes to the heart of physics.

By 1994, the theorists had concluded that the semileptonic branching fraction of the b-hadron of less than 12% was difficult to accomodate within the confines of the Standard Model. Although the measurements by the experiments at higher energy LEP facility were consistent with the theory within errors, the measurements at lower energy facilities were lower than the expectation as summarized in Table 1.3. The attempts to lower the theoretical value to accomodate the measurements of the lower energy facilities did not prove fruitful.

The difference between the two sets of experiments is in the composition of the decaying b-hadrons. At lower energies, only B^+, B^0 and their charge conjugate mesons, collectively denoted as B, are produced in nearly equal amounts and decayed. At LEP, where the available energy is much higher, b-baryons as well as b-mesons, collectively denoted as H_b, are produced in rough percentages of $B^+ : B^0 : B_s^0 : b\text{-baryons} = 40\% : 40\% : 10\% : 10\%$. The composition of the decaying b-hadrons needs to be taken into account when comparing the measured values between higher and lower energy experiments. The $\mathcal{B}_{\mathrm{SL}}$ measurements of the LEP experiments reflect the branching fraction of the b-hadrons, $\mathrm{BR}(b \to X\ell)$. The measurements of the lower energy experiments, however, are the branching fraction of the B mesons, $\mathrm{BR}(B \to X\ell)$. Considering that the semileptonic branching fraction of the b-baryons is expected and

measured to be smaller than that of b-mesons, the gap between the two sets of measurements is actually wider than it looks in the Table 1.3.

1.2 Current status

Since the crisis in 1994, some breakthroughs have been made. Further calculations have shown that the semileptonic branching fraction can be lowered. This breakthrough, however, accompanies a condition; it demands that a quantity called the charm count, n_c, be higher than the previous expectation. The charm count refers to the number of weakly decaying charm or anticharm hadrons in the decay of one b-hadron. Figure 1.1 shows the theoretical bounds of this condition along with the newly calculated semileptonic branching fraction, $\mathcal{B}_{SL}$.

The results from the lower energy experiments still remain outside the theoretical bounds. To reconcile the differences in the measurments of $\mathcal{B}_{SL}$ between the higher and lower energy facilities, new analyses are conducted by the LEP experiments. The emerging results of the new analyses show an alarming situation, as they inch toward the edge of the theoretical limits and the measurements of the lower energy experiments. These new results are listed in Table 1.4. This unsettling situation has sparked

Table 1.3 Published measurements of semileptonic branching fraction by various experiments

E_{CM} (GeV)	Experiment	$\mathcal{B}_{SL}$ (%)[a]	Reference
LEP $M(Z) \approx 92$	ALEPH	$11.20 \pm 0.33 \pm 0.42$	[2]
	DELPHI	$11.30 \pm 0.45 \pm 0.68$	[3]
	L3	$11.42 \pm 0.48 \pm 0.37$	[4]
	OPAL	$10.60 \pm 0.60 \pm 0.66$	[5]
$M(\Upsilon(4S)) \approx 10.6$	CLEO	$10.49 \pm 0.17 \pm 0.43$	[6]
	ARGUS	$9.7 \pm 0.5 \pm 0.4$	[7]

[a]While the measurements at LEP experiments reflect $BR(b \to X\ell)$, those shown for the lower energy experiments are $BR(B \to X\ell)$.

interests and new ideas. Some, though not popular, discount the discrepancy by stating that the calculations involving strong interaction are not precise enough to indicate a problem. Nevertheless, studies into possible enhancement of specific hadronic decay channels are ongoing to try to account for the decrease in the semileptonic channel.

1.3 Strategy

As noted in the previous section, the measurements of the semileptonic branching fraction by the LEP experiments are being updated from the previously published values. It is important to have a closer look into the reasons for updating the measurements since the emerging numbers are alarmingly close to the edge of the theoretical bounds. The obvious reason for the update is more data, thereby reducing the statistical uncertainties in the measured values. However, a more important reason is the improvement of analysis techniques. The traditional methods by which the semileptonic branching fraction is measured require a complex fitting algorithm which measure, along with the semileptonic branching fraction, b- and c-quark production fractions, the fragmentation functions and the forward-backward asymmetries. This global fitting approach results in large inter-dependency among the measured values, and the accuracy of each measurement becomes questionable.

The newer methods take advantage of the ability to isolate the events in which primary b-quarks are produced in the collision of e^+e^-. By selecting only the b-quark events and identifying the leptons in those events, semileptonic decays of b-hadrons can be easily isolated. This method, however, does not lead to an easy analysis. As shown in Figure 1.2, leptons can be produced in more than one way in the decay of a b-hadron. The leptons produced directly in a weak decay of a b-quark $b \rightarrow qW^-$

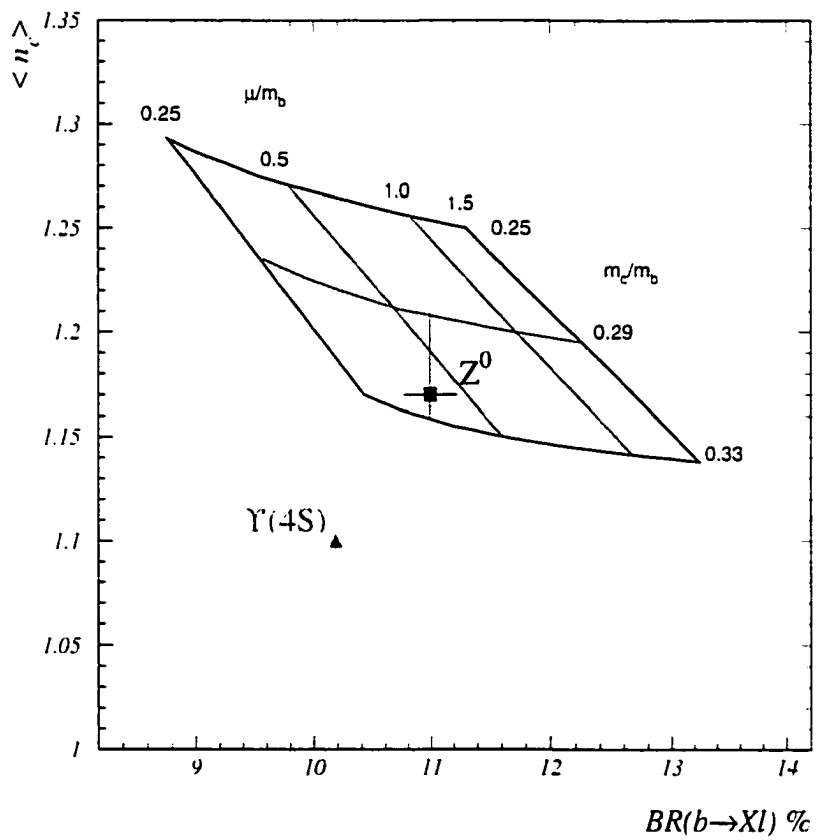

Figure 1.1 Comparison between the theoretical bounds of $\mathcal{B}_{SL}$ and n_c and the published experimental results from CLEO and LEP collaborators. The $\Upsilon(4S)$ result has been adjusted from $BR(B \to \ell X)$ to $BR(b \to \ell X)$.

Table 1.4 Newer measurements of $\mathcal{B}_{SL}$ from the LEP experiments

Experiment	$\mathcal{B}_{SL}$ (%)	Reference
DELPHI	$10.73 \pm 0.08 \pm 0.60$	[8]
L3	$10.16 \pm 0.13 \pm 0.30$	[9]
OPAL	$10.83 \pm 0.10 \pm 0.30$	[10]

and $W^- \rightarrow \ell^- \bar{\nu}$ [2], are referred to as the direct or primary leptons, and the leptons produced in a weak decay of a secondary quark are referred to as the secondary or cascade leptons. The semileptonic decay branching fraction concerns the production of the primary leptons. The difficult part of the analysis, then, is separating the primary leptons from the secondary leptons. One solution is to examine the lepton momentum, as the primary leptons tend to have higher momenta than the secondary leptons. This method, however, relies heavily on the theoretical models to determine the shape of the primary and the secondary lepton momentum spectra.

A better solution to separate the primary leptons from the secondary leptons is to exploit the charge difference of primary and secondary leptons. As indicated in Figure 1.2, the sign of the electric charge of the primary lepton is the same as that of the decaying b-quark; whereas the opposite can be said about the seconary leptons. The strategy, then, is to find the charge of the b-quark in the decaying b-hadron and to match the sign of the charge to that of the lepton. Same sign will indicate a primary lepton, and opposite sign will indicate a secondary lepton. This method, however, does have a small problem. Primary leptons are not the only same–sign leptons. As shown in Figure 1.3, the charmed quark produced from a W in a weak decay of a b-quark can decay semileptonically. The leptons produced in this process are referred to as the upper–vertex leptons and have the same–sign charge as in the case of primary leptons. The upper–vertex leptons are expected to be small in number as compared

[2]The processes shown thoughout this thesis imply charge conjugate states as well, unless noted otherwise. The charge conjugate reaction for this process is $\bar{b} \rightarrow \bar{q}W^+, W^+ \rightarrow \ell^+\nu$.

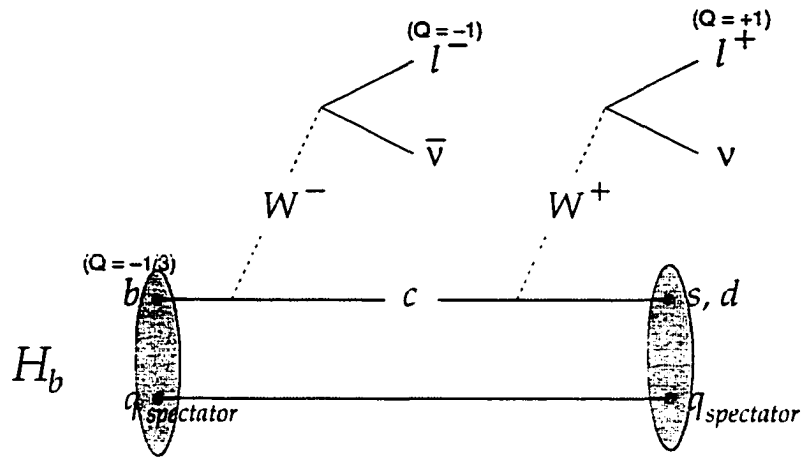

Figure 1.2 Charge correlation method

to other type of leptons and have lower momenta. Thus the momentum spectrum can be used as a tool with which the upper–vertex leptons are distinguished from the primary leptons.

The plots in Figure 1.4 show the expected momentum spectra for same–sign and opposite–sign leptons (electrons or muons) in the rest frame of decaying b-hadron. The same–sign spectra are composed of the spectrum for the primary leptons and for the upper–vertex leptons. By using this method, the branching fraction for each leptonic mode can be measured. The measurement of the branching fraction for the upper–vertex leptons will be the first measurement of its value and will be of great interest. The measured value, if above expectation, will indicate an enhancement of a hadronic decay channel in the decay of the b-hadron and will aid in explaining the lower semileptonic branching fraction.

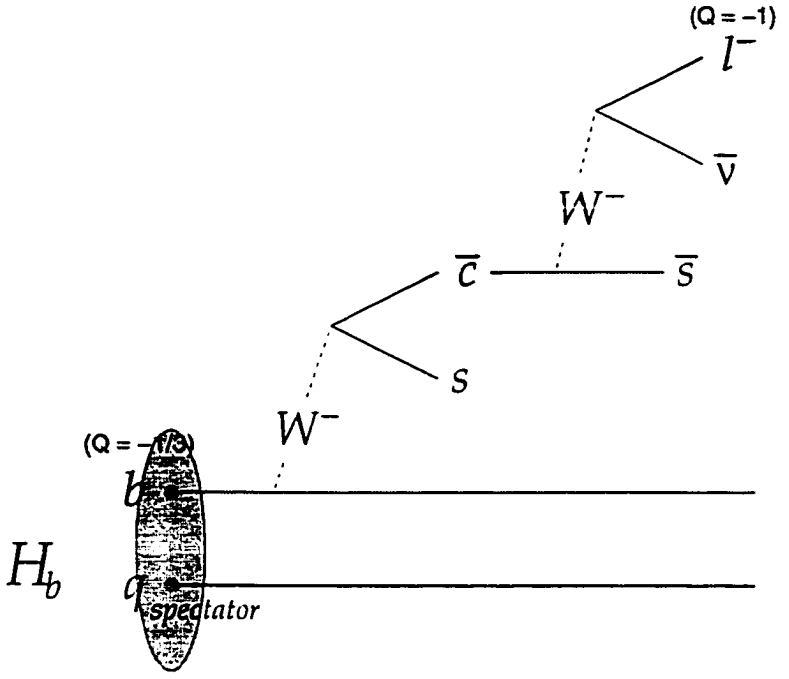

Figure 1.3 Same-sign leptons in the upper–vertex decay

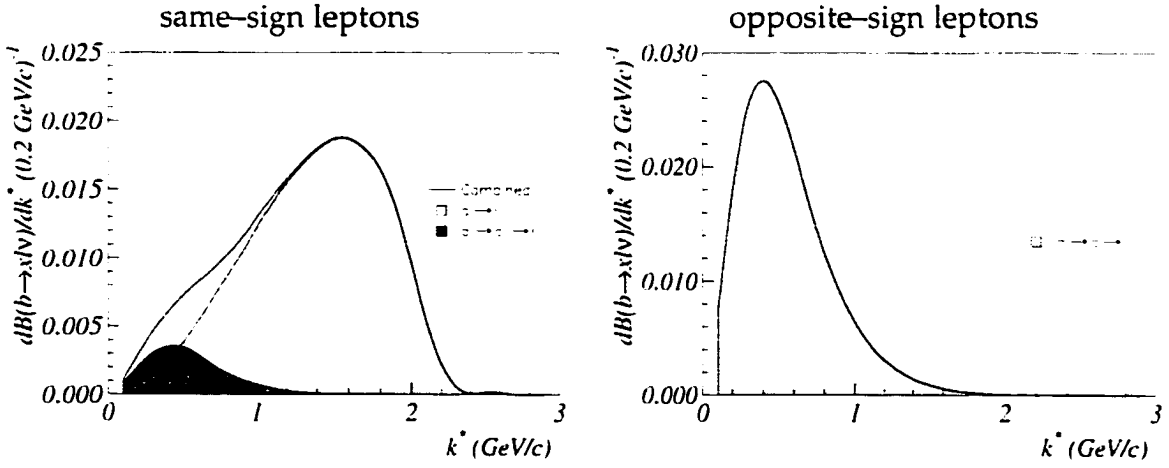

Figure 1.4 Expected momentum spectra for same–sign and opposite–sign leptons

1.4 Outline

What follows is a detailed description of the process and the results of the analysis of the inclusive semileptonic branching fraction of a b-hadron using the data collected by the DELPHI detector during the 1994 and 1995 running periods. The details on the theory are presented in Chapter 2. The experimental facilities including DELPHI are described in Chapter 3. The analysis procedure and the results are presented in Chapters 4 and 5. And the concluding thoughts are shown in Chapter 6. The results of this analysis and three other analyses conducted by other DELPHI groups have been published [8].

2 THEORETICAL POINT OF VIEW

Looking at the weak decay of the b-hadron in the simplest way, it is possible to treat the b-quark in the hadron as a free particle, which decays by producing a virtual W. In this case, the semileptonic branching fraction, $\mathcal{B}_{SL}$, simply refers to the fraction at which the virtual W produces any lepton pair. The possible decay products of W are the three generations of leptons and two generations of quarks as shown in Figure 2.1. If the masses of the final state products are ignored and equal weight is given to each of the lepton pairs and the three color modes of the quark pairs, the semileptonic branching fraction for each lepton pair would simply be $\frac{1}{9}$ from counting. This obviously agrees very well with the measured value. So, can it be this simple?

The answer is no since there are other effects that need to be included in the calculation. However, the assumption that only the b-quark participates in the decay is a good starting point. This assumption is known as the spectator model, which refers to the non-participating quark. The result calculated from this simple model will be the base from which corrections will be made. One of the corrections will be to account for the interaction between the decaying b-quark and the spectator quark. Another correction will deal with a possible enhancement of $W \rightarrow \bar{c}s$ or $b \rightarrow c\bar{c}s$. These corrections, all of which are complicated and have sizeable uncertainties, will bring the calculated $\mathcal{B}_{SL}$ down. However, the resulting increase in the hadronic decay modes needs to be confirmed.

The theoretical knowledge can aid in experimentally measuring $\mathcal{B}_{SL}$ by predicting the shape of the lepton energy spectrum. As explained in the previous chapter,

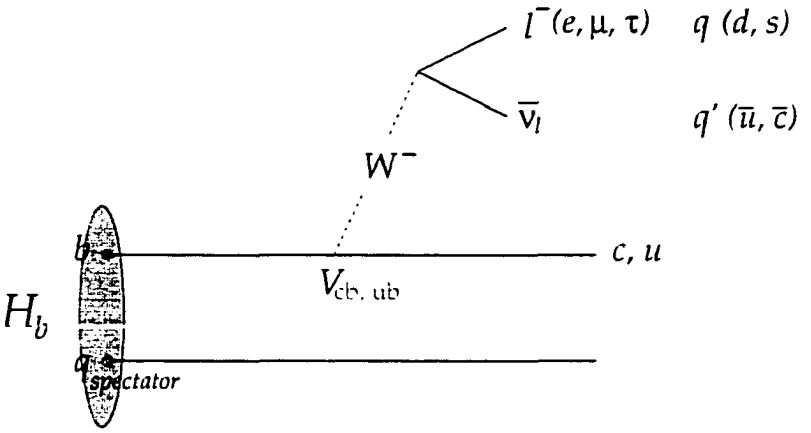

Figure 2.1 Decay of a b-hadron in the spectator model

the lepton spectrum can be used to separate primary leptons from secondary leptons; the primary leptons can then be used to measure $\mathcal{B}_{SL}$. In general, there are two approaches to calculating the shape of the spectrum: inclusive and exclusive. The inclusive approach treats the b-hadron system at the quark level, similar to the calculation of $\mathcal{B}_{SL}$ as above. The exclusive approach takes advantage of the final hadronic states that are saturated by a few resonant states. The sum of these exclusive final hadronic modes is then used as the shape of the primary leptonic spectrum. There are some differences in the shapes of the spectra between the inclusive and exclusive approaches. These differences will ultimately lead to a model-dependent uncertainty in the measurement of $\mathcal{B}_{SL}$.

The following sections detail the calculational processes described above to obtain $\mathcal{B}_{SL}$ and the leptonic spectra. So far, the use of the word lepton has followed its strict definition, referring to any member of the three generations of leptons shown in Table 1.1 or their anti-partners. However, for the ease of describing experimental data and theoretical calculations, from this point, a lepton, $\ell^{\pm}$, will refer only to $e^{\pm}$ and $\mu^{\pm}$. Any other use of the word will be explicitly stated.

2.1 The basics and the dilemma

In the study of inclusive semileptonic decay, the main concern is not of the individual hadronic decay channels but of the sum of all the possible final state hadrons. The study simply ignores the detailed contribution of each decay channel that contributes to the semileptonic rate. There are definite experimental and theoretical advantages of such a study. Experimentally, a complex step of reconstructing hadrons resulting from the decay can be avoided, while only an easy task of observing leptons is required. Theoretically, complex calculations involving quark-to-quark interactions or that involving gluons are not considered. By treating the b-quark as a free particle as in the spectator model, the knowledge of the weak interaction is the only necessity to start the calculational process.

To begin the calculation of $\mathcal{B}_{\mathrm{SL}}$, a mathematical definition is needed. Keeping in mind that the interest is in the inclusive mode—sum of all exclusive modes—and that the semileptonic branching fraction refers to the fraction of the direct process which produces a lepton out of all the decay possibilities, $\mathcal{B}_{\mathrm{SL}}$ is defined as

$$\mathcal{B}_{\mathrm{SL}} = \frac{\sum_X \Gamma(H_b \to X\ell^-\nu)}{\Gamma(H_b \to \mathrm{all})}, \tag{2.1}$$

where X is either a c-hadron or a u-hadron and ℓ refers to either an e or a μ. Since the mass of the τ is much greater than that of $e^{\pm}$ or $\mu^{\pm}$, the case of τ is treated separately and is beyond the scope of this study.

In the case of simple spectator model as in Figure 2.1, Equation 2.1 can be approximated as

$$\mathcal{B}_{\mathrm{SL}} \approx \frac{\sum_X \Gamma(b \to X\ell^-\nu)}{\Gamma(b \to \mathrm{all})}. \tag{2.2}$$

Also from the figure, all the important decay channels can be accounted for, and the

denominator is approximated. The result is

$$\mathcal{B}_{SL} \approx \frac{\Gamma_\ell}{2\Gamma_\ell + \Gamma_\tau + \Gamma_{had}}, \tag{2.3}$$

where

$$\Gamma_\ell = \Gamma(b \rightharpoonup c\ell^-\bar{\nu}),$$

$$\Gamma_\tau = \Gamma(b \rightharpoonup c\tau^-\bar{\nu}),$$

$$\Gamma_{had} = \Gamma(b \rightharpoonup c\bar{u}d) + \Gamma(b \rightharpoonup c\bar{c}s).$$

It should be noted that the above equation ignores contributions from $b \rightharpoonup uW^*$ decays, other rare processes, such as penguin decays, and the small difference in phase space between $e^\pm$ and $\mu^\pm$. Rewriting the above equation in the units of Γ_ℓ,

$$\mathcal{B}_{SL} \approx \frac{1}{2 + r_\tau + r_{\bar{u}d} + r_{\bar{c}s}}, \tag{2.4}$$

with $r_\tau = \frac{\Gamma_\tau}{\Gamma_\ell}$. To further this calculation, a knowledge of partial decay width is needed. This can be borrowed from a general process in which a free quark, Q, decays to another quark, q, and produces a pair of fermions, $f_1 f_2$, by the means of virtual W: $Q \rightharpoonup qW^*, W^* \rightharpoonup f_1\bar{f}_2$. The partial decay width of this process is [11]

$$\Gamma(Q \rightharpoonup qf_1\bar{f}_2) = \Gamma_0 N_C |V_{qQ}|^2 |V_{f_2 f_1}|^2 I(\frac{m_q}{m_Q}, \frac{m_{f_1}}{m_Q}, \frac{m_{f_2}}{m_Q}), \tag{2.5}$$

where $\Gamma_0 = G_F^2 m_Q^5 / 192\pi^3$, the number of colors, $N_C = 3$ for hadronic decays and 1 for semileptonic decays, and V_{xy} is the corresponding CKM matrix element. From this equation, what contributes to the calculation of $\mathcal{B}_{SL}$ in Equation 2.4 is the difference in phase space calculation, $I(x, y, z)$, among the different decay modes. Since I is dependent on the masses of the particles involved, the choice of mass is particularly important for hadronic decays, where the definition and measurement of a quark mass bear ambiguities. Nevertheless, with a choice of $m_b = 4.8$ GeV$/c^2$, $m_c = 1.5$ GeV$/c^2$, $m_s = 0.3$ GeV$/c^2$ and $m_u = m_d = 0$, along with the color factor, gives

$\frac{r_{\bar{u}d}}{3} \approx 3$ and $\frac{r_{\bar{c}s}}{3} \approx 0.31$. A better knowledge of the decay into τ gives $r_\tau \approx 0.20$. These numbers lead to an overestimate of $\mathcal{B}_{SL}$ at 16%.

The calculation is not by any means complete at this point. There are two sizable issues that need to be dealt with. The first issue is how the interaction among the quarks affect $\mathcal{B}_{SL}$. The second one is to determine the appropriate input values for the quark masses. The perturbative QCD corrections, the interaction among the quarks, address the exchange of hard gluons between the quarks in the decay. This perturbative correction was carried out by Altarelli and Petrarca [12] and was shown to enhance the hadronic channel, r_{had} in Equation 2.4, by a factor of about 1.27, and decrease $\mathcal{B}_{SL}$:

$$\mathcal{B}_{SL} \approx \frac{1}{2 + r_\tau + 1.27(r_{\bar{u}d} + r_{\bar{c}s})} \approx (14.4 \pm 0.45(\text{scale}) \pm 0.8(\alpha_s))\%. \qquad (2.6)$$

As for the issue of quark mass, the ambiguities in the measurement of quark mass are taken into account. Altarelli and Petrarca argued that by using the lower bounds of the quark masses: $m_b = 4.6\ \text{GeV}/c^2$, $m_c = 1.2\ \text{GeV}/c^2$, $m_s = 0.15\ \text{GeV}/c^2$ and $m_u = m_d = 0$, $\mathcal{B}_{SL}$ can be lowered to about 12.2% with the same uncertainties as above [12]. By stretching the uncertainties in the above calculation and the uncertainties in the measurement, the two can be considered consistent at their limits. However, this is not a comforting situation. Furthermore, it has been argued that there may be sizable QCD corrections, both perturbative and non-perturbative, that were not taken into account in the above calculation.

Such arguments have led to a different approach to solve this problem. A relatively recent approach is by applying the heavy-quark effective theory (HQET) in the calculation of $\mathcal{B}_{SL}$. HQET is suitable for a hadron system composed of one heavy quark and light quark(s). The argument dictates that the heavy quark, Q, moves nonrelativistically and its momentum equals that of its lighter partner, q:

$$|\mathbf{p}_Q| = |\mathbf{p}_q| \sim \Lambda_{had} \sim \Lambda_{QCD}, \qquad (2.7)$$

where $\Lambda_{QCD} \approx m_{proton}/3 \approx 330\text{Me}V$ and a typical interaction scale for a hadron $\Lambda_{had} \sim 200\text{–}300\ \text{Me}V$. The associated velocity transfer to the heavy quark is

$$|\mathbf{v}_Q| = \frac{|\mathbf{p}_Q|}{m_Q} \sim \frac{\Lambda_{had}}{m_Q}. \tag{2.8}$$

Therefore, in the limit $m_Q \gg \Lambda_{had}$, the heavy quark is essentially stationary. With that as the starting point, the internal properties and the decays of the hadron are expressed as a systematic expansion in terms of $1/m_Q$. The advantage of HQET over the hadron models used in the calculation above is that the expansion is derived directly from the fundamental theory of QCD. This leads to the uncertainties being easier to identify and estimate.

The application of this approach to the semileptonic decay of b-hadrons is natural as both the initial and final state hadrons contain a heavy quark: $b \to W^* c$. By treating the b-quark as a stationary decay source, the lowest order term in the HQET expansion is found to be the same as the spectator model:

$$\Gamma(B \to X) = \Gamma(b \to x) + \mathcal{O}(1/m_b^2) \tag{2.9}$$

In their work, Bigi *et al.* [1] have argued that the corrections, $\mathcal{O}(1/m_b^2)$, would likely be small and that an enhancement of nonleptonic rate would come from perturbative corrections. They have concluded that $\mathcal{B}_{\text{SL}}$ must satisfy the bound

$$\mathcal{B}_{\text{SL}} \geq 12.5\%. \tag{2.10}$$

The results from both approaches agree. They are, however, not consistent with measurements of the lower energy experiments. This has led Bigi *et al.* to declare the situation baffling [1]. They have suggested among others an intervention by "New Physics" to aid in explaining this situation. Before a drastic approach such as that is taken, there are still yet some missing pieces in the perturbative analysis and a possible enhancement in hadronic decay channels that deserve more attention.

2.2 Any ideas?

Since the crisis described above became known, several attempts have been made to explain the measurements that are lower than the calculated values. There are mainly two schools of thought, both of which represent ideas to increase hadronic decays. One suggests the enhancement of final state c-hadrons. Bagan *et al.* suggested an increase of $b \rightarrow c\bar{c}s$, or $b \rightarrow W^{*-}c$ and $W^{*-} \rightarrow \bar{c}s$, by about 35% after their next-to-leading order calculation of the process [13]. This approach reduced $\mathcal{B}_{SL}$ to about 11% but increased the charm count, n_c, to about 1.3. The average of measured charm count, however, stood at or below 1.1. The solution to this dilemma may come from invalidating the previous misconception that $\bar{c}s$ produced from W^* in the decay $b \rightarrow W^*c$ hadronize only into D_s. This previous belief was questioned by Buchalla and Dunietz [14] after their calculation showed that there was sizable phase space available to produce two c-hadrons in such a decay. Observing a significant enhancement of the suggested decay mode of $\bar{B} \rightarrow D\bar{D}\bar{K}X$ would increase n_c. This decay mode is currently sought after by numerous experiments.

The second school of thought is to increase hadronic decays without enhancing the final state c-hadrons. It suggests a large contribution from $b \rightarrow s + gluon$ [15]. If such a large contribution occurs, there should be an excess amount of high momentum kaons in the decay of b-hadron. Preliminary indications from CLEO suggest that such an excess does not exist. In contrast, an indication of enhancement in $b \rightarrow c\bar{c}s$ is detected both by CLEO and ALEPH [16], and these preliminary measurements are used in composing the simulation sample for the upper–vertex leptons in this analysis.

2.3 Leptonic energy spectrum

As demonstrated above, the calculations involving hadronic decays remain the main stumbling block in the calculation of $\mathcal{B}_{SL}$. On the experimental side, the shape of the leptonic energy spectrum is required in a typical analysis. Theoretically, this task is a little more manageable than the exact calculation of $\mathcal{B}_{SL}$. However, the calculation of the leptonic energy spectrum is not without difficulties. The difficulty involves the calculation of the hadronic current, which cannot be solved from the first principle as the lack of knowledge in the non-perturbative QCD sector prevents exact calculation. It is possible, however, to treat the problem phenomenologically. The hadronic current, which represents the coupling of W to the quarks, can be treated either inclusively or exclusively. Inclusive approach treats the b-hadron at the quark level and is independent of the final hadronic states. Exclusive approach, in contrast, assumes that the decay of b-hadron is saturated by only a few resonant final hadronic states.

2.3.1 Inclusive approach

The inclusive approach in a model proposed by Altarelli, Cabibbo, Corbò, Maiani and Martinelli (ACCMM) [12] puts an emphasis on extracting the CKM matrix elements, namely V_{cb} and V_{ub}, from inclusive lepton spectra by employing a QCD-corrected parton model. The internal dynamics of the decaying meson is characterized by a Gaussian distribution, $\phi(p)$, representing the momentum of the heavy quark:

$$\phi(p) = \frac{4}{\sqrt{\pi} p_F^3} e^{-\vec{p}^2/\vec{p_F}}, \tag{2.11}$$

where the Fermi momentum parameter, p_F, determines the width of the distribution. While the spectator quark has a definite mass, m_{sp}, the heavy quark, b-quark in this

case, is assumed to be a virtual particle with its mass, m_b, constrained by the conservation of energy and momentum:

$$m_b^2 = m_B^2 + m_{sp}^2 - 2m_B\sqrt{m_{sp}^2 + p^2}, \tag{2.12}$$

where m_B is the mass of the meson. The free parameters in this model are: width of the distribution, p_F, the mass of the spectator, m_{sp}, and the mass of the daughter particle, whether a c- or a u-quark. The decay distribution is then boosted from the b-quark rest frame to the decaying meson rest frame. For the semileptonic process, the energy spectrum of the lepton is

$$\frac{d\Gamma(m_b, x)}{dx} = \frac{G_F^2|V_{cb}|^2 m_b^5}{96\pi^3}[\Phi(x,\epsilon) - G(x,\epsilon)], \tag{2.13}$$

where $x = 2E_\ell/m_b$, $\epsilon = m_c/m_b$ and neglecting $b \to uW$ mode. The function $\Phi(x,\epsilon)$ describes the free quark decay distribution:

$$\Phi(x,\epsilon) = \frac{x^2(x_m - x)^2}{(1-x)^3}[(1-x)(3-2x) + (1-x_m)(3-x)] \tag{2.14}$$

with $x_m = 1 - \epsilon^2$, and $G(x,\epsilon)$ is a correction function that describes the effects of gluon radiation. This correction incorporates both the initial gluon radiation and the virtual gluon exchange or the vertex correction. While the complicated correction function only slightly changes the spectrum for most of the x range, its significance is pronounced from its logarithmic divergence at the endpoint region, where $x \to x_m$. The endpoint region continues to be problematic, even with numerous approaches in the context of HQET. Despite this problem, the spectrum can be calculated over much of the momentum range, and the result is shown in Figure 2.2.

2.3.2 Exclusive approach

A few final resonant states saturate the semileptonic decays of b-hadrons, according to the exclusive models. These states, neglecting $b \to u\ell\nu$, include the ground

state, D meson, the first excited state, D^* meson, and the higher states, collectively known as D^{**}. The hadronic current is constructed from available four-vectors, the momenta and the spin–polarization vectors. In the case of pseudoscalar decaying to another pseudoscalar, $P(Q\bar{q}) \rightarrow P'(q'\bar{q})\ell\nu$, such as the case of $B \rightarrow D\ell\nu$, the axial vector does not contribute to the hadronic current. Therefore, the hadronic current is

$$< P'(p')|V^\mu|P(p) > = F_1(q^2)[(p+p')^\mu - \frac{M^2 - m_{P'}^2}{q^2}q^\mu] + F_0(q^2)\frac{M^2 - m_{P'}^2}{q^2}q^\mu, \tag{2.15}$$

where $q = p - p'$, $V^\mu = \bar{q}'\gamma^\mu Q$ and the Lorentz–invariant form factors $F_0(0) = F_1(0)$. In the semileptonic case, where $m_\ell \rightarrow 0$ is a good approximation, $q^\mu L_\mu = 0$ leads to

$$< P'(p')|V^\mu|P(p) >= F_1(q^2)(p+p')^\mu. \tag{2.16}$$

The case of a pseudoscalar decaying to a vector meson, $P(Q\bar{q}) \rightarrow V(q'\bar{q})\ell\nu$, as in the case of $B \rightarrow D^*\ell\nu$, is a bit more complicated since each term must be linear in the polarization vector, ε, of the vector meson. This leads to the hadronic current of

$$< V(p',\varepsilon)|V^\mu - A^\mu|P(p) > = \frac{2i\epsilon^{\mu\nu\alpha\beta}}{M+m_V}\varepsilon_\nu^* p'_\alpha p_\beta V(q^2) - (M+m_V)\varepsilon^{*\mu}A_1(q^2) + \frac{\varepsilon^*\cdot q}{M+m_V}(p+p')^\mu A_2(q^2), \tag{2.17}$$

where $A_1(q^2)$ and $A_2(q^2)$ are the form factors. The form factors are functions of the four-momentum transfer, q^2, between the initial and the final state mesons and are unknown. Each exclusive model chooses its own convenient q^2 to calculate the form factors and extrapolate to other values of q^2.

Among the different models to estimate the form factors, the model of Isgur, Scora, Grinstein and Wise (ISGW) [17] is most readily accepted by a number of experiments. In this model, nonrelativistic approximations are made to describe the decay of b-mesons, owing to the heaviness of the b-quark. And at the minimum recoil of the final

state meson, which is at the maximum momentum transfer, q^2_{max}, the form factors are approximated from a Coulomb-plus-linear form for the potential:

$$V(r) = -\frac{4\alpha_s}{3r} + br + c. \tag{2.18}$$

When extrapolating to more problematic larger recoils with lower q^2, an exponential form of the form factors is assumed along with an ad hoc factor for relativistic corrections, κ. The resulting form factors have the following form and q^2 dependence:

$$F_i(q^2) \approx F(q^2_{max}) exp(\frac{q^2 - q^2_{max}}{\kappa Q^2}). \tag{2.19}$$

After determining $\kappa = 0.7$ from measured pion form factors, the relative branching fractions are calculated to be 27%, 62% and 11% for the decays of $B \to D\ell\nu$, $B \to D^*\ell\nu$ and $B \to D^{**}\ell\nu$, respectively. The shape of the overall semileptonic momentum spectrum of ISGW is compared with that of ACCMM in Figure 2.2. The contributions of individual decay modes to the overall ISGW semileptonic momentum shape are shown in Figure 2.3.

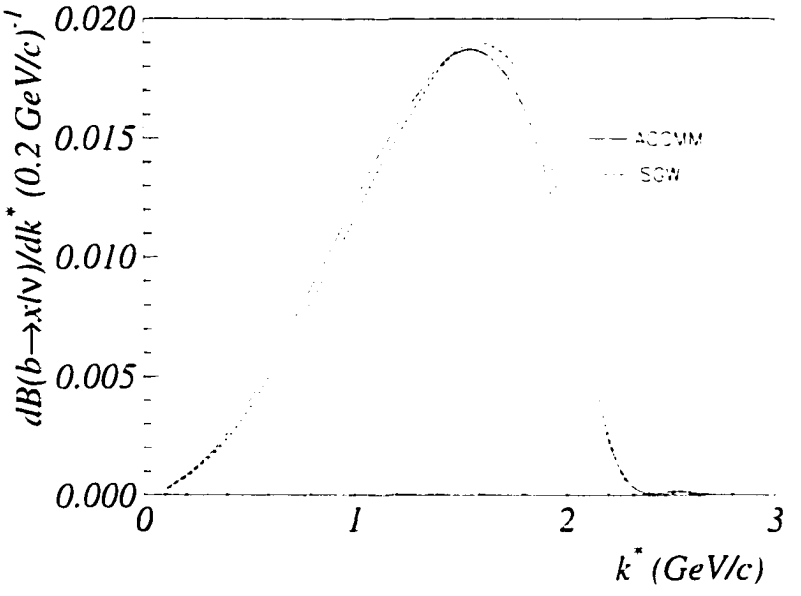

Figure 2.2 Comparison among the different theoretical models. The inclusive model, ACCMM, is compared with the exclusive model, IGSW.

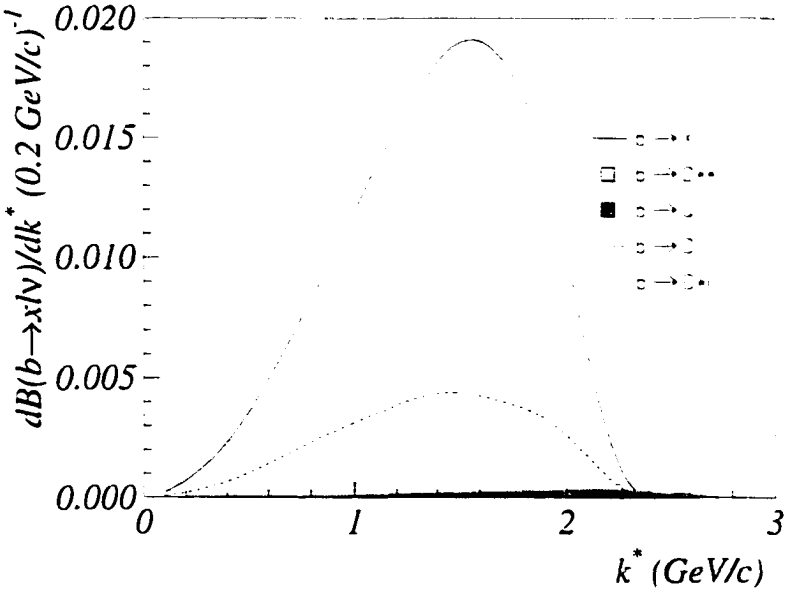

Figure 2.3 Contributions of different decay modes to $\mathcal{B}_{SL}$ in the ISGW model

3 HARDWARE AND PERFORMANCE

To study the physics of particle interactions, two major ingredients are needed: one to create and collide particles and another to see what happens when the particles collide. Both of these ingredients are found at the European Organization for Particle Research (CERN) through a series of particle accelerators and detectors. Its flagship apparatus is the Large Electron-Positron (LEP) storage ring. The seventeen-mile long LEP storage ring is at about 100 meters under a land that divides the French region of Pay de Gex and the Swiss canton of Geneva. Equipped with accelerating and focusing devices, LEP provides head-on collisions of electrons and positrons at four detector locations. One of the detectors is the DEtector with Lepton, Photon and Hadron Identification (DELPHI). DELPHI, as shown in Figure 3.1, contains the world's largest superconducting magnet and elaborate subdetectors for excellent tracking and particle identification abilities. In the following sections, LEP and DELPHI are briefly described. The subdetectors, which directly affect this analysis, are described in detail.

3.1 The LEP collider

LEP is the final stage of the acceleration process of electrons and positrons before collision. As depicted in Figure 3.2, electrons and positrons begin their lives in Linear Accelerators (LINAC). The 200 MeV electrons from the LEP Injector Linac (LIL) are made to collide with a high Z target; the collision produces positrons of about

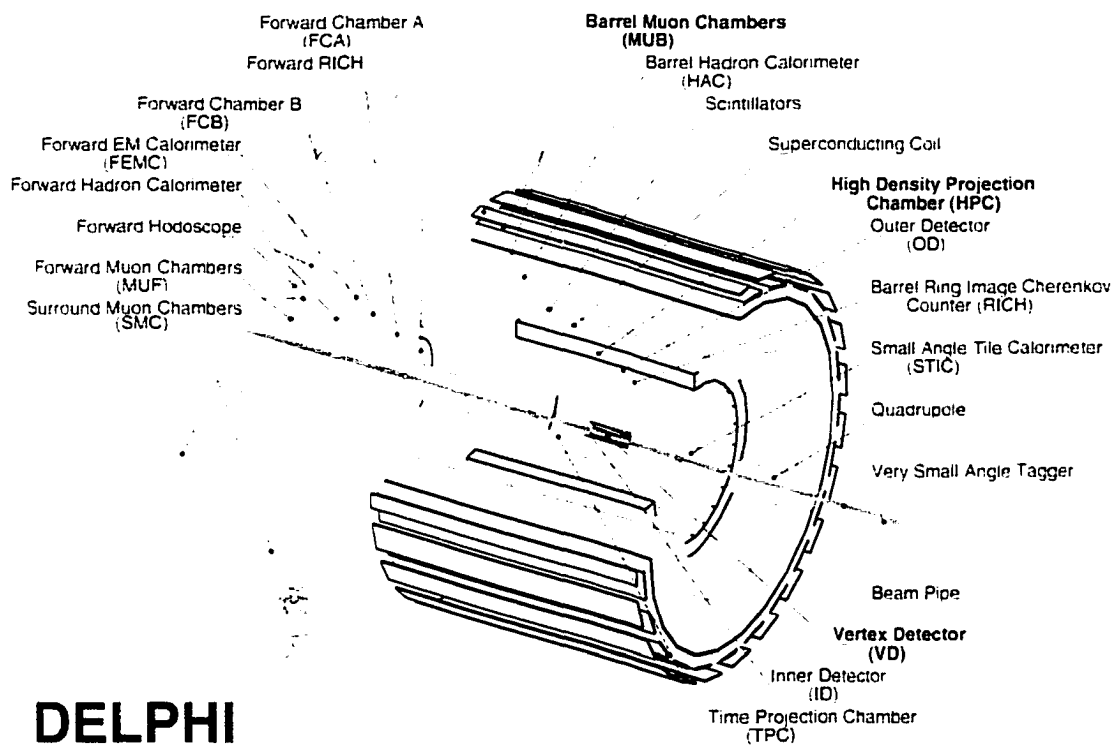

Figure 3.1 DELPHI detector is shown with an average sized human for comparison. The barrel section and one of the two endcaps are shown in the diagram. The components which are important to this analysis are highlighted.

10 MeV in energy from pair-production. These positrons and 10 MeV electrons from an electron gun are accelerated to 600 MeV by the second stage LIL before the Electron Positron Accumulator (EPA) stores and stacks them into bunches. The EPA then injects the bunches to the Proton Synchrotron (PS) which accelerates the bunches to 3.5 GeV. This process is followed by the Super Proton Synchrotron (SPS) which after accelerating the bunches to 20 GeV injects the bunches into the LEP storage ring.

Using high frequency cavities, the bunches are accelerated to 45 GeV in the LEP ring. The amount of energy lost in synchrotron radiation from bending the beams around the circular structure is

$$\Delta E = -8.85 \times 10^{-5} \frac{E^4}{r} \frac{m}{GeV^3} \tag{3.1}$$

per revolution, where r is the radius of the curvature. This amounts to about 120 MeV of energy loss for a beam energy of 45 GeV. When the beams are made to collide at the detector locations, the process of

$$e^+e^- \rightarrow \gamma, Z^0 \rightarrow \text{anything} \tag{3.2}$$

takes place. With the center of mass energy being equal to the mass of the Z^0, an ideal environment is created that enhances the intermediate Z^0 state over γ in the above process according to Figure 3.3. The event rate can be obtained by combining the total cross section, σ, for the above process with the luminosity, $\mathcal{L}$:

$$\frac{dN}{dt} = \sigma \mathcal{L}. \tag{3.3}$$

The luminosity is typically $10^{31} cm^{-2} s^{-1}$, calculated from

$$\mathcal{L} = \frac{N^+ N^- k_N f_{rev}}{4\pi \sigma_x \sigma_y}, \tag{3.4}$$

where $N^{\pm}$ are the numbers of $e^{\pm}$ in each bunch, which are about 4.2×10^{11}, k_N is the number of bunches in each beam, 8, f_{rev} is the circulation frequency, $11.25kHz$, and $\sigma_{x,y}$ are the horizontal and vertical widths of the beam, $\sim 200 \times 10\mu m$.

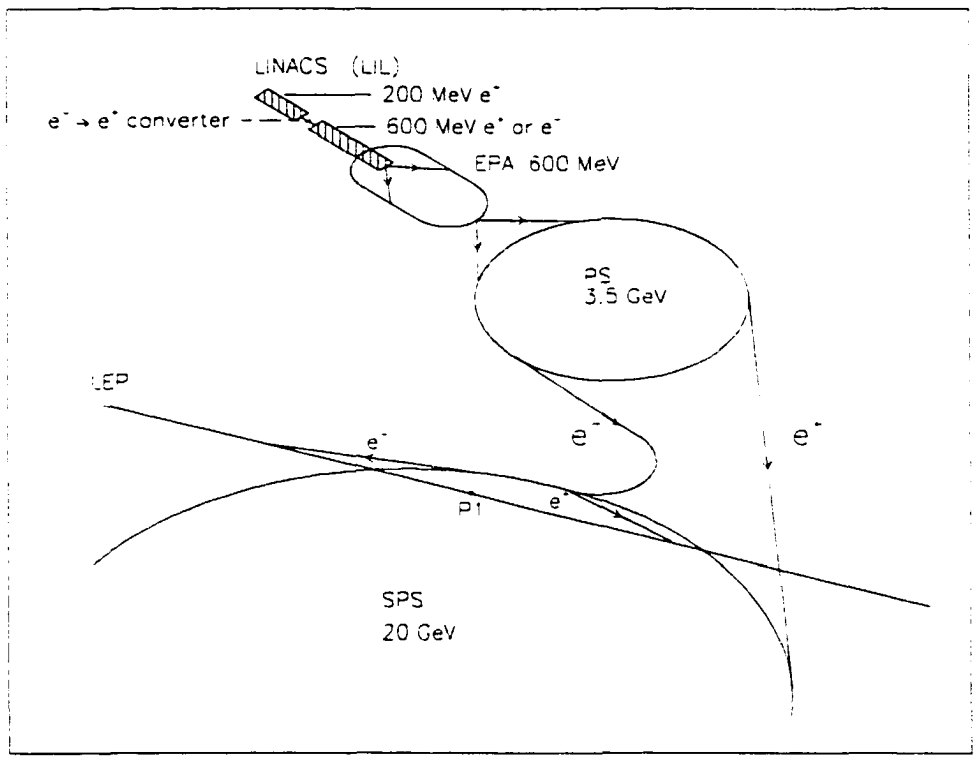

Figure 3.2 Particle acceleration procedure

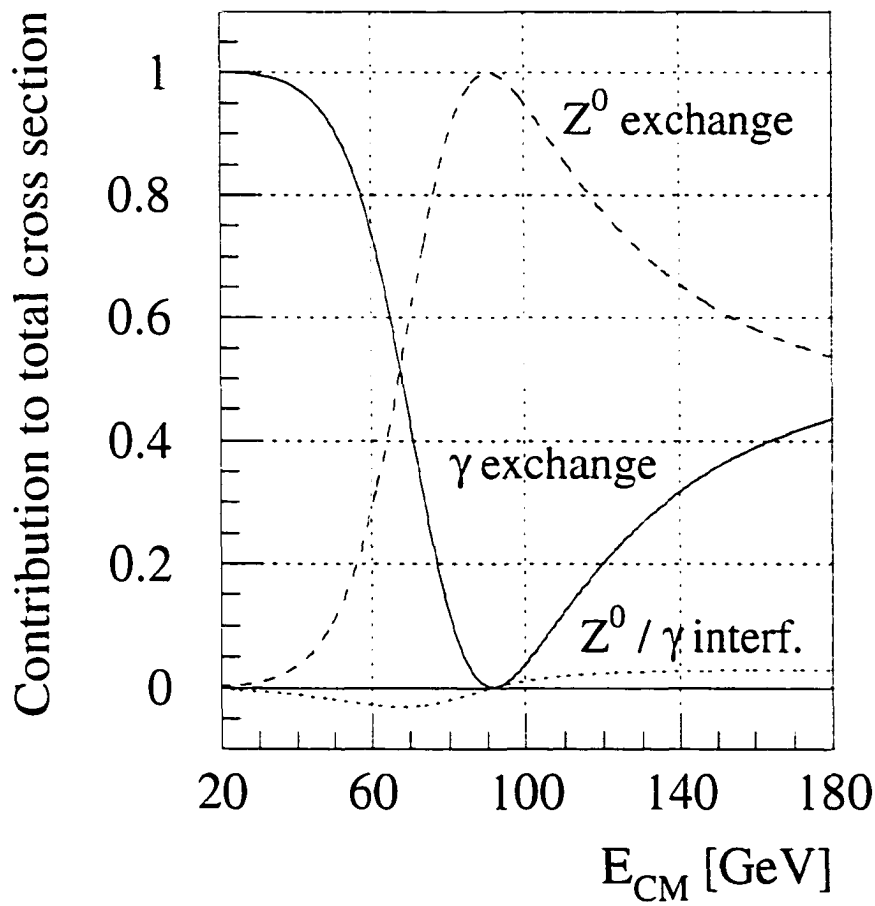

Figure 3.3 Contribution to the total cross section in the process of $e^+e^- \rightarrow \gamma, Z^0 \rightarrow$ anything. Adapted from [18]

3.2 The DELPHI detector

Sitting along the beam axis, the cylindrically shaped DELPHI measures ten meters long and nine meters in diameter with the collision region at the center. This marvel of engineering and physics was built by an international collaboration involving approximately 500 physicists from over 15 countries. Iowa State University is the sole US member the collaboration. DELPHI employs a coordinate system that is based at the center of the detector, where the e^+e^- collisions take place, as the origin and the z-axis in the direction of the e^- beam. The directions of x- and y-axes are toward the center of LEP and up, respectively. A cylindrical coordinate system is often used, as well, with x-y plane forming $r\phi$. The polar angle to the z-axis, when a spherical system is used, is θ.

The DELPHI detector is designed to cover the full 4π range. In this analysis, however, only the barrel section is used because of its superior tracking abilities. The range of the barrel section around the collision region is $40^\circ - 140^\circ$ in θ. As this analysis is confined to that region, the descriptions of the endcaps are not shown here. The general description and the specifics of the endcaps can be found in [19]. In the following subsections, a collision and the subsequent decay are first described. Then, the details of reconstructing tracks and identifying particles, particularly electrons and muons are presented. The description of triggering and data acquisition follows. Much of the following information, particularly those concerning the specifications of DELPHI subdetectors are taken from [19] and are not exclusively cited.

3.2.1 Event topology

An event refers to any data taken by DELPHI. The data may be of a cosmic ray passing through the detector, a result of the circulating beam interacting with residual gas in the LEP ring, or a result of e^+e^- collision. Further, the result of e^+e^- collision

with Z^0 intermediate state can be either leptonic or hadronic events. The leptonic events are easily identified over the hadronic events because of their simple topology: two energetic back-to-back tracks[1]. The hadronic events are the result of the Z^0 decaying into a quark and an antiquark and have a large number of tracks, typically 20 charged tracks per event, as illustrated in Figure 3.4. Since the events of interest for this analysis are the hadronic events, the following description of the event topology is limited to those events.

With the center of mass energy equal to the Z^0 mass, an e^+e^- collision is followed by the creation of a Z^0 state at rest which decays immediately to a quark, q, and an antiquark, $\bar{q}$, back-to-back. The location of the Z^0 decay is referred to as the primary vertex. The q and $\bar{q}$, under the influence of the strong force, immediately radiate additional quarks and gluons in a process called fragmentation. The fragments then hadronize into colorless hadrons. Most of the unstable hadrons produced immediately decay into stable ones, producing tracks from the primary vertex. In the case of $Z^0 \rightarrow b\bar{b}$, the b-hadrons have a long and measurable lifetime as compared to other unstable hadrons. The points at which the b-hadrons decay are therefore separated from the primary vertex and are referred to as secondary vertices. A simple illustration of this type of event is shown in Figure 3.5. Tracks that originate from the primary vertex are called the fragmentation tracks, and the ones originating from the secondary vertices are called the secondary tracks. In this analysis, the secondary vertices and tracks are referred to as b vertices and tracks.

It is convenient to divide the events into two hemispheres. Figure 3.5 shows an example of such a case. A hemisphere containing one b-hadron and its decay products can be separated from the other hemisphere to analyze the decay of one b-hadron at

[1]Because τ's decay in flight, the observed topology for τ's is more complicated.

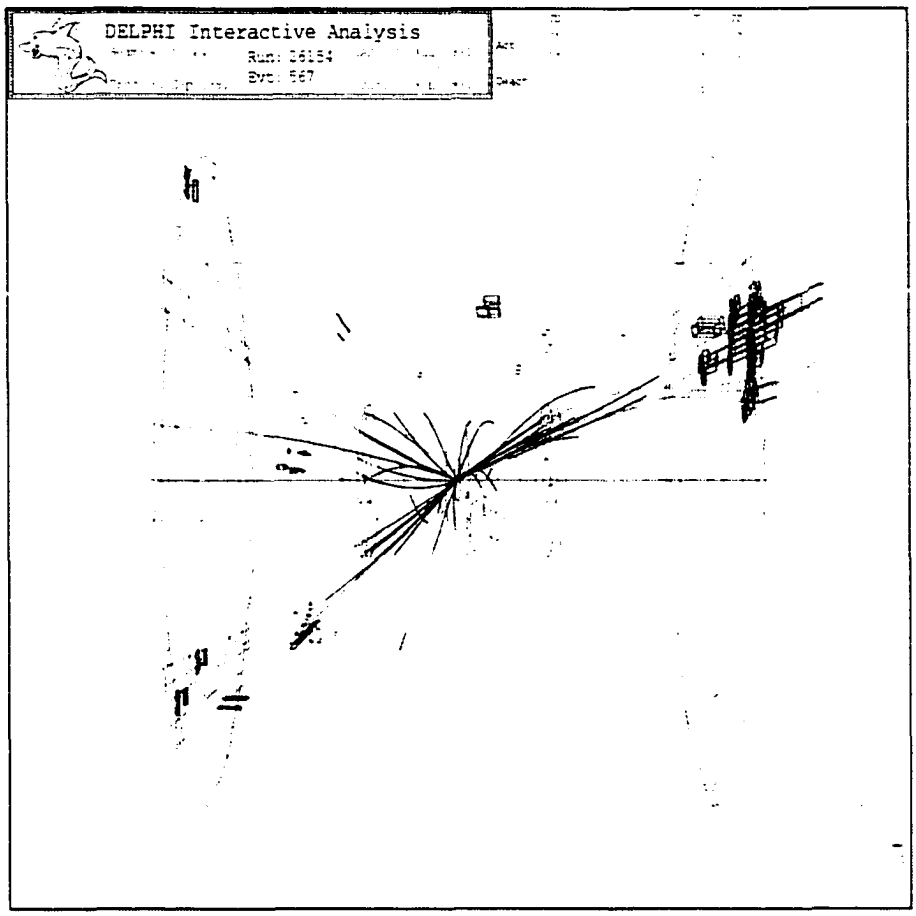

Figure 3.4 Three-dimensional view of a hadronic event

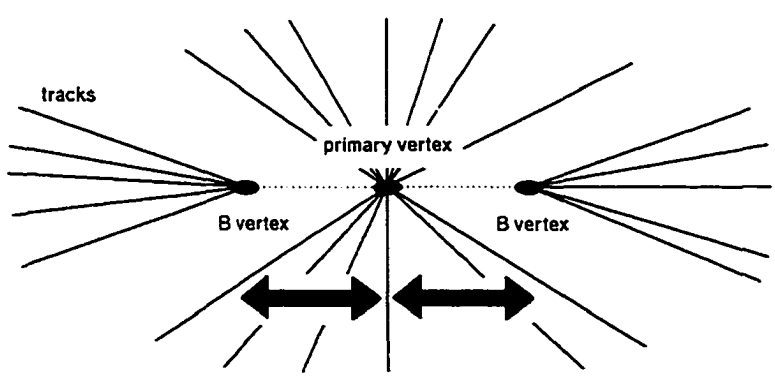

Figure 3.5 A simple representation of a *b* event. The *b*-hadron vertices are separated from the primary vertex.

a time. For this purpose, the event thrust axis is defined with thrust, $\mathcal{T}$:

$$\mathcal{T} = \frac{\mathrm{Max} \sum_{i=1}^{n} |\vec{p}_i^{\,\parallel}|}{\sum_{i=1}^{n} |\vec{p}_i|}, \tag{3.5}$$

where $|\vec{p}_i^{\,\parallel}|$ is the longitudinal momentum of i-th track, either charged or neutral, with respect to the thrust axis. The thrust axis is chosen such that the above quantity is maximized. The plane perpendicular to the thrust axis divides an event into the two hemispheres and the primary vertex.

3.2.2 Reconstructing tracks

In a superconducting coil at 4.5°K, 5000 A of current creates 1.23 T of uniform magnetic field in the direction of the beam axis. This allows an accurate determination of the momentum of a charged particle as it follows a circular trajectory in the magnetic field. In the barrel section of DELPHI, the tracks are reconstructed by combining the information from four independent subdetectors: the microvertex detector, the time projection chamber, the inner and outer detectors.

As heavy charged particles, such as protons and pions, pass through matter, their energies are lost, and their tracks, though minimally, can be deflected. This is mainly the result of inelastic collisions with the atoms in the material. For highly energetic particles, hard collisions lead to ionization. The amount of lost energy in the ionization is small compared to the kinetic energy of the particle. However, the high number of collisions in the matter lead to a substantial loss of energy. Most tracking devices measure the tracks by collecting the ionization electrons.

The momentum resolution by combining the information from all the tracking subdetectors is determined in colinear $Z^0 \rightarrow \mu^+\mu^-$ events to be

$$\sigma(1/p) = 0.57 \times 10^{-3} (\mathrm{GeV}/c)^{-1} \tag{3.6}$$

in the barrel section. The following subsections describe each of the tracking subdetectors in detail.

3.2.2.1 Microvertex detector

Located closest and parallel to the collision region and the beam pipe, the microvertex detector (VD) is three concentric layers of silicon strip detectors as shown in Figure 3.6. The layers are located at the radii of 6.3, 9.0 and 10.9 cm and named closer, inner and outer layers, respectively. While the inner layer is composed of single-sided silicon strips, the strips in the closer and outer layers are double-sided, one side orthogonal to the opposite side. This provides, along with the measurements in $r\phi$, the measurements in z-direction. The polar angle coverage for a charged particle hitting all three layers is $44° < \theta < 136°$ and for the closer layer is $25° < \theta < 155°$. The resolution in $r\phi$ is about 8 μm and in z is about 9 μm for tracks perpendicular to the detectors.

3.2.2.2 Time projection chamber

As the main device for tracking information, the time projection chamber (TPC) is cylindrically shaped with the length of 260 cm and is situated between the radii of 29 cm and 122 cm. Up to sixteen space points help to reconstruct a track in the polar region of $39° < \theta < 141°$. However, tracks can be reconstructed using four space points up to the polar region of 21° and 159°. The resolutions are $\sigma(r\phi) = 250\mu m$ and $\sigma(z) = 880\mu m$ with two-point resolution being about $1cm$.

As shown in Figure 3.7, the TPC consists of two cylindrical drift shells. Charged tracks that pass through the TPC volume filled with 80:20 mixture of argon:methane leave ionization trails. In each half, an electric field of 187 V/cm, parallel to the magnetic field, directs the ionization electrons toward the endcap. Any diffusion from having to drift a relatively large distance is reduced by the magnetic field, which confines the electrons to the drift direction. By using the arrival times of the ionization electrons, tracks can be fully reconstructed. The end-plates are divided into six az-

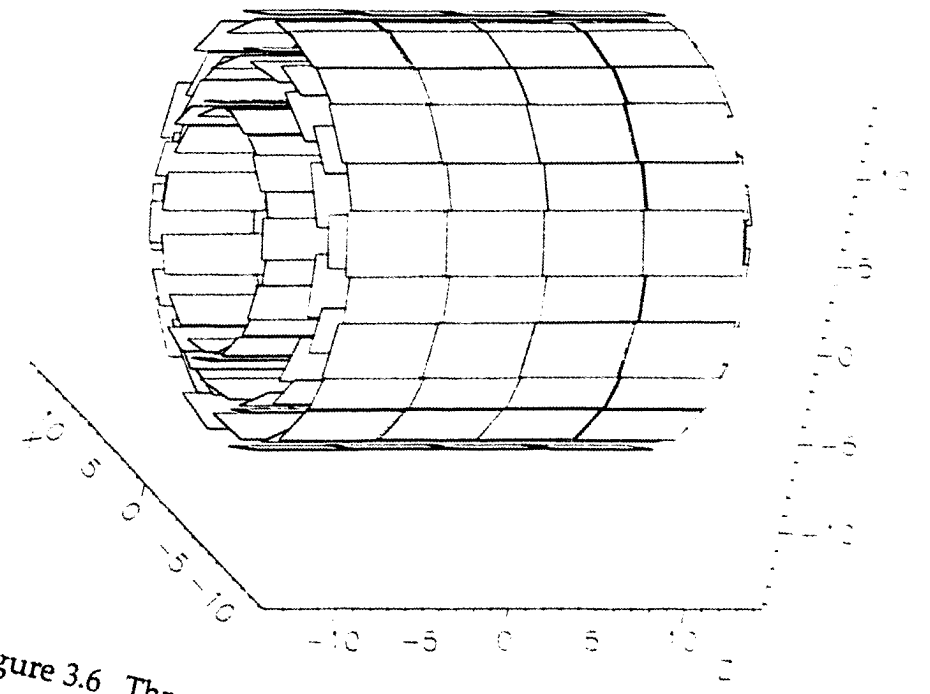

Figure 3.6 Three concentric layers of microvertex detector

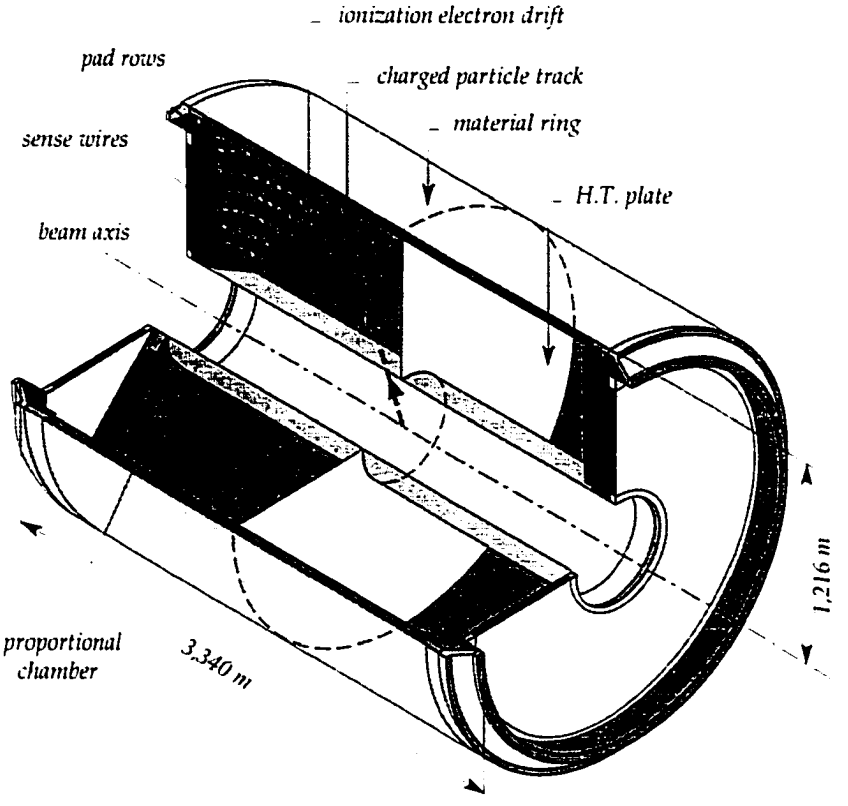

Figure 3.7 TPC is shown with a charged particle passing through.

imuthal sectors, each of which contains 192 sense wires and 16 concentric pad rows. This provides up to 16 space points per track.

3.2.2.3 Additional tracking components

In addition to VD and TPC, the inner and outer detectors provide tracking information. The inner detector (ID), situated between the radii of 12 cm and 28 cm, is composed of two concentric layers. The inner layer is divided into 24 azimuthal sectors of jet drift chambers, providing 24 $r\phi$ points per track. Surrounding the inner layer are five layers of multi-wire proportional chambers, which provide tracking information in z coordinate as well as in $r\phi$. The angular acceptance in θ for both the drift and proportional chambers is $30° < \theta < 150°$. With the angular resolutions of $\sigma(r\phi) = 50\mu m$ and $\sigma(\phi) = 1.4mrad$, a track with as little as $1mm$ in separation from other tracks can be distinguished.

The outer detector (OD) is the outermost tracking device, sitting between the radii of $198cm$ and $206cm$. Its tracking information is important especially for high momentum tracks, whose curvature is not as pronounced as others. The OD consists of five layers of drift cells, three of which are equipped to provide z coordinate information. It is divided into 24 overlapping azimuthal modules. The polar angle coverage is $42° < \theta < 138°$. The angular resolution is $\sigma(r\phi) = 110\mu m$, and the resolution in z is $\sigma(z) = 3.5cm$.

3.2.3 Particle identification

As the paths of tracks are reconstructed by measuring the ionization electrons in the TPC, the energy loss of the passing charged particles can also aid in revealing the identity of the particle. The average differential energy loss (dE/dx) of the track, also called the stopping power, depends on the speed of the particle, as $1/\beta^2$ fac-

tor dominates the energy loss equation, or Bethe-Bloch formula [18]. The stopping power reaches its minimum at the speed $\beta \approx 0.97$ and slowly increases as *beta* increases. This region of minimum dE/dx is known as the minimum ionizing region, and the particles that lose energy close to the minimum are called the minimum ionizing particles, or mip's. The dependence of dE/dx on the momentum of a particle, as measured by TPC, is shown in Figure 3.8. Above 2 GeV/c, pions and kaons can be separated at above the 1σ level.

The ring imaging Čerenkov detector (RICH) employs another technique for identifying particles. As a charged particle travels through a dielectric medium, if its velocity is greater than the local phase velocity of light, a cone of Čerenkov light is emitted, whose emission angle, Θ_{ch}, depends on the velocity of the particle. Combining this velocity measurement with the momentum measurement of each particle, the particle mass can be determined. The RICH subdetector has two radiators with different refractive indices. Particle identification for momentum range below 8 GeV/c is done in the liquid radiator, and above 2.5 GeV/c is done in the gas radiator. Figure 3.9 shows the Čerenkov angle as a function momentum.

The measurements of dE/dx and Čerenkov angle are combined to provide the particle identification. An example of this highly effective process can be seen in Figure 3.10, where kaon tracks can easily be distinguished from others. The identification of particles plays an important role in determining the charge of the b-quark in the decaying b-hadron, as will be discussed in the next chapter. It is therefore crucial for both TPC and RICH to be in perfect operational condition for this analysis to be successful.

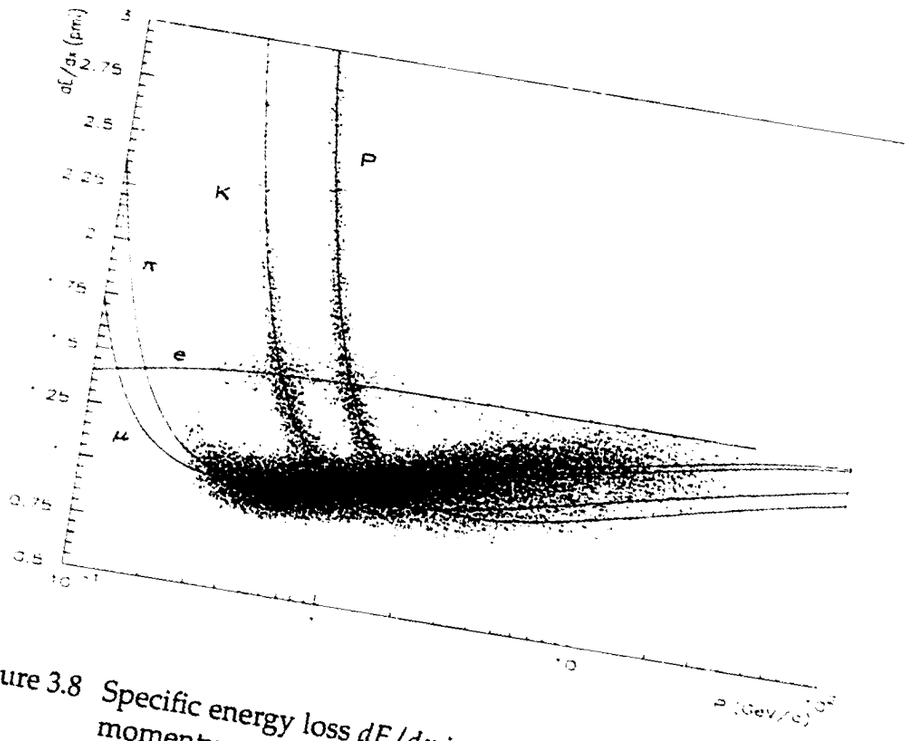

Figure 3.8 Specific energy loss dE/dx in the TPC as a function of particle momentum.

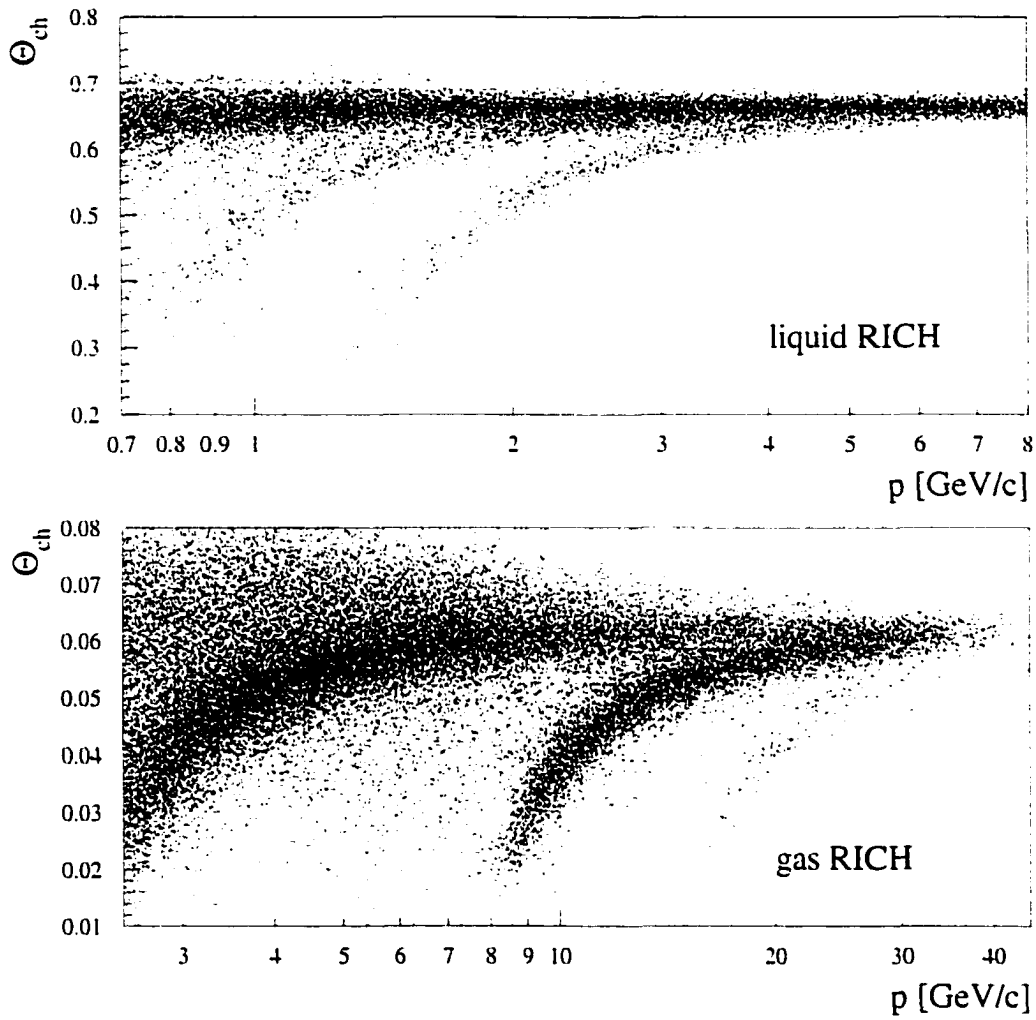

Figure 3.9 Average Čerenkov angle per track as a function of momentum in the Barrel RICH. The three bands in the plots correspond to pions, kaons and protons from left to right.

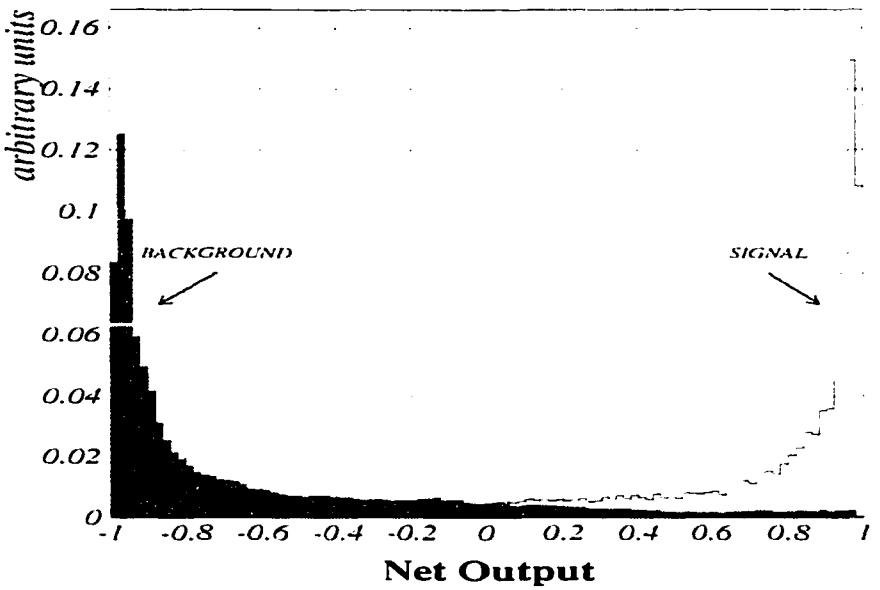

Figure 3.10 Kaons are separated from other particles using dE/dx and Čerenkov angle measurements. Adapted from [20].

3.2.4 Detection of electrons

Similar to heavy charged particles, electrons and positrons do lose energy in matter by ionization. However, this process becomes less important to the overall energy loss at high energies. The dominant energy loss for high energy $e^{\pm}$ comes from bremsstrahlung and rises linearly with energy. Bremsstrahlung refers to the electromagnetic radiation emitted by an electron in the influence of the electric field of a nucleus. The contributions of the two processes to the fractional energy loss of $e^{\pm}$ are illustrated in Figure 3.11. The energy at which the loss rates from the ionization and by bremsstrahlung are equal is quite low at ~ 7 MeV and is called the critical energy.

The photons created from bremsstrahlung predominantly convert to $e^{+}e^{-}$ pairs, the process known as pair production. This process combined with bremsstrahlung creates electromagnetic showers. There are two statistical observations that help to characterize the electromagnetic showers. The first is that each electron or positron with energy greater than the critical energy undergoes bremsstrahlung process within

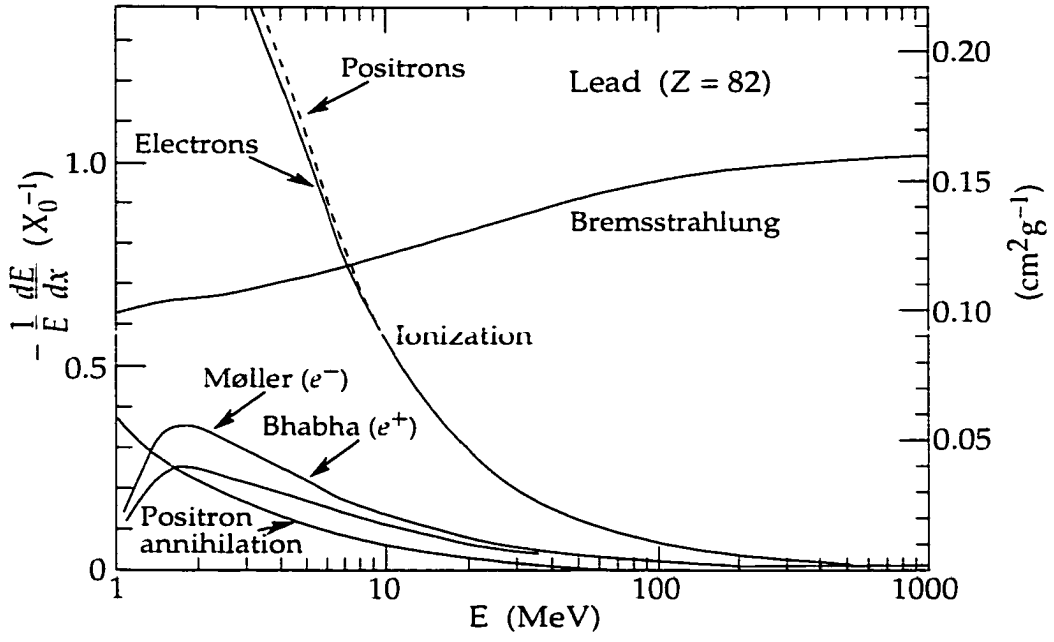

Figure 3.11 Fractional electron energy loss per radiation length as a function of e^+e^- energy. Adapted from [18].

one radiation length, where the radiation length is defined as the distance over which the electron energy is reduced to $1/e$ of its original energy from radiation. The second observation is that a photon converts to an e^+e^- pair also within one radiation length. With these observations, the number of particles can easily be calculated after t radiation lengths from shower initiation:

$$N(t) = 2^t, \tag{3.7}$$

each with average energy of $E(t) = E_0/2^t$, where E_0 is the energy of the shower initiator. The cascade of e^+e^- and photons stops when the energy of the $e^\pm$ reaches the critical energy. An overly simplified illustration of an electromagnetic shower can be seen in Figure 3.12. This simple approach is used to build calorimeters, such as the high-density projection chamber in DELPHI.

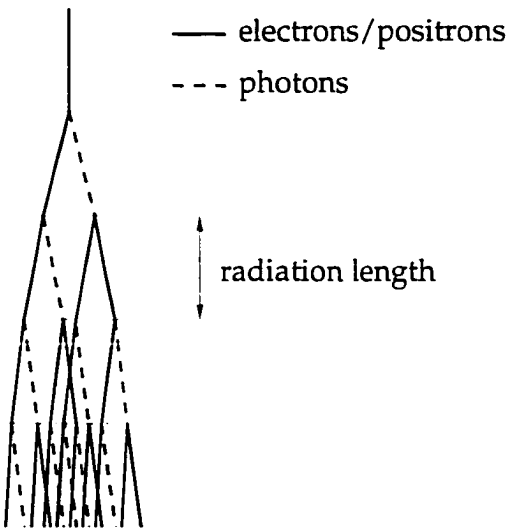

Figure 3.12 Overly simplified illustration of electromagnetic cascades.

3.2.4.1 High density projection chamber

The high-density projection chamber (HPC) is located between the radii of 208 and 260 cm. It consists of six 24 azimulthally arranged modules along z for a total of 144 modules. Each module is a time projection chamber with 40 layers of lead. Except for a trigger counter layer, the layers are separated by 8 mm gaps filled with argon/methane mixture. The electromagnetic showers are initiated in the layers made out of lead wires, and the ionization electrons are drifted by the electric field of 106 V/cm created by the lead wires. With each layer being 3 mm, the total converter thickness is from 18 to 22 radiation lengths depending on the polar angle. For each module, 128 read-out pads are grouped into 9 parallel rows. Each of the first 3 rows covers the range of 3 drift gaps, the middle 3 rows cover 4 drift gaps each, and the last 3 rows cover 6 drift gaps each. This configuration can be seen in Figure 3.13. The resolutions are determined from Bhabha events as $\sigma_\phi = 15mrad$ and $\sigma_z = 5mm$.

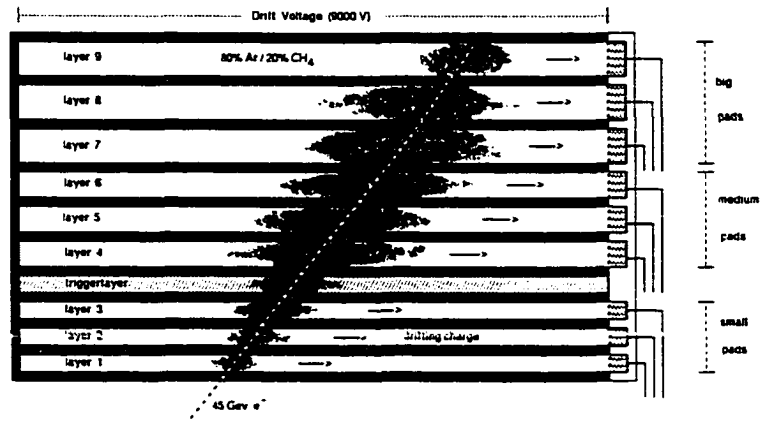

Figure 3.13 The nine-pad row configuration is shown for a single HPC module.

3.2.4.2 Selection of electrons

Any charged track with its polar angle within the acceptance region of the HPC is considered as an electron candidate. Imposing the minimum momentum of 3 GeV/c on the candidates eliminates the region of momenta where a reliable efficiency calculation is not possible due to heavy contamination of charged hadrons, mostly pions. Electron probability for each track is then calculated based on the measurements from the TPC, the HPC and the RICH subdetectors [21]. Using simulated leptons, a momentum-dependent cut on the electron probability is calculated to provide a constant efficiency for selecting electrons of 65% over the entire momentum range.

The efficiency for identifying electrons from this technique is measured by examining two data samples. For the momentum of less than 12 GeV/c, converted photons are used by tagging one of the e^+e^- and selecting the other to be analyzed. For higher momentum range, compton events are used by assuming the most energetic neutral and charged particles are photon and electron candidates. In addition, misidentification probability, or probability of selecting a hadron as an electron, is measured by selecting events with lower b-tagging probability, thereby removing electrons from semileptonic decays, and rejecting electrons from photon conversion by requiring

at least one hit in the VD. The electrons in the selected sample amount to less than 1%. The misidentification probability is found to be $(0.40 \pm 0.02)\%$ for 1994 and $(0.38 \pm 0.04)\%$ for 1995 data.

3.2.5 Detection of muons

Muon detectors are usually found farthest from the collision point. The DELPHI muon detectors are not an exception to this rule. The reason for this is that muons are the only charged particles, if sufficiently energetic, that can traverse the lead and iron calorimeters unaffected. This provides the first level of separation between muons and hadrons. Even after this filtering, some hadrons, punch-through from hadronic showers, do penetrate to the muon detectors. The situation is more bleak when considering the high ratio of charged hadrons to prompt leptons in hadronic events. Fortunately, muons can be extracted by using the accurate tracking information and precise position measurements from the muon chambers.

3.2.5.1 Muon chambers

The outer-most subdetector, the muon chambers (MUB), are comprised of 1,372 drift chambers arranged in 24 azimuthal sectors. Each sector is composed of inner, outer and peripheral modules. The inner module with three layers of 14 total chambers is embedded in the hadron calorimeter. The arrangement of the modules in one sector is shown in Figure 3.14. The polar coverage is $53° < \theta < 127°$. The azimuthal coverage is hermetic with peripheral modules covering the gaps in the other modules in the adjoining sectors. The precision in $r\phi$ is $3mm$ for each chamber.

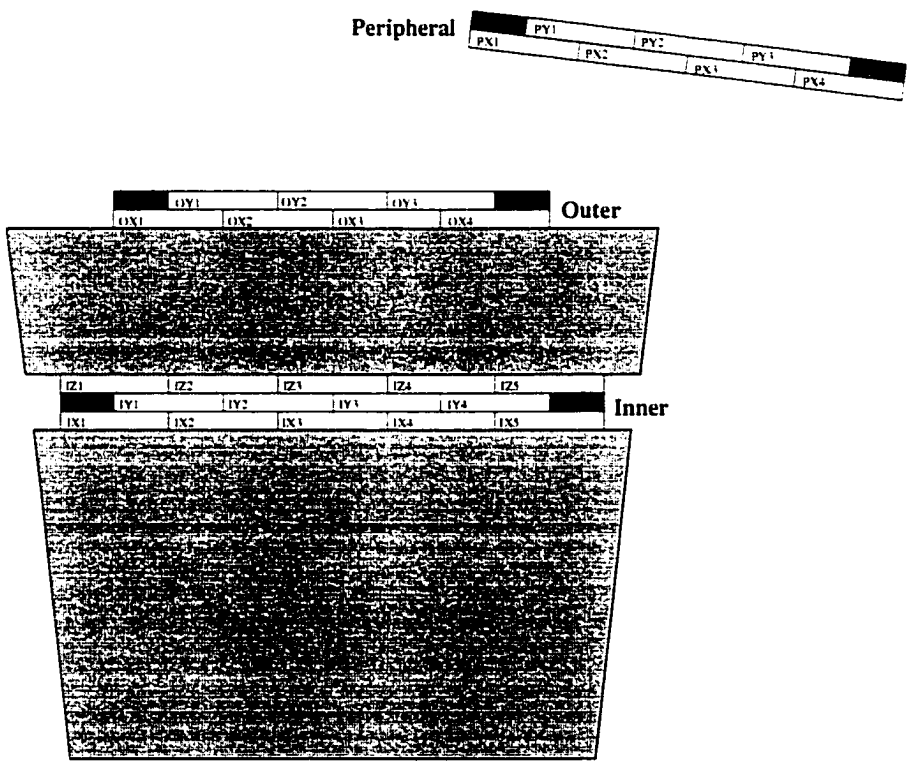

Figure 3.14 Arrangement of 3 modules of muon chambers in one sector. There are 24 of such modules.

3.2.5.2 Selection of muons

As in the case of electrons, a minimum momentum of 3 GeV/c is required to be a muon candidate. The polar angle requirement, $|cos\theta| < 0.62$, excludes the region of poor geometrical acceptance. The muon identification process relies on the extrapolation of the tracks to the position measurements by the MUB, as a larger deviation in the track extrapolation is found for hadrons and the inflight decays of hadrons. The goodness of the fit to the extrapolation is used to rate the confidence of muon tracks. The muons are selected for this analysis such that the mean efficiency of the identification is about 82% with little dependency on the momentum and the polar angle.

The efficiency for identifying muons is measured by examining $Z \rightarrow \mu^+\mu^-$ events, decays of τ into muons and the two photon collisions, $\gamma\gamma \rightarrow \mu^+\mu^-$. The misidentification probability is studied in the anti b-tagged events, as in the electron case above. Since the punch-through hadrons cannot be disentangled from muons, the amount of real muons are estimated from a simulation sample and are subtracted to obtain hadron-only sample. The misidentification probability is found to be $(0.52 \pm 0.03)\%$ for 1994 and $(0.53 \pm 0.03)\%$ for 1995 data.

3.2.6 Triggering and data acquisition

To identify potentially interesting events for readout, DELPHI employs a trigger system, comprised of four successive levels, T1, T2, T3 and T4, of increasing selectivity. In typical operation, eight bunches of electrons and positrons circulate at equal distances apart at LEP, and the bunch crossings occur every 11 μs. The decisions of the first two levels, T1 and T2, take 3.5 μs and 39 μs, respectively, after the Beam Cross Over (BCO) signal. This implies that for each positive decision from T1, the immediately following three BCOs are lost. The later two levels, T3 and T4, are asynchronous

with the BCO and are software filters that reduce the background by approximately half at each level.

The first level trigger, T1, considers only simple patterns in track chambers, scintillation counter hits and low energy single clusters in calorimeters. The main source of background for T1 is the random noise from the subdetectors. To reduce this background, the correlation among the subdetectors is introduced in the second level, T2. In addition, T2 utilizes the data from detectors with long drift times. Each positive T2 decision triggers acquisition of the data collected by the Front End Buffers (FEBs).

Without introducing additional algorithm or correlation among the subdetectors, T3 validates the decision made by T2. By applying calibration constants, sharper thresholds in the energy showers are set, and tigher cuts are made on pointing tracks toward the primary vertex. The purpose of the final level trigger, T4, is to tag Z decays in real time. This software filter checks the quality of the data by testing the source of the data on the basis of individual subdetectors. It rejects events if no track points toward the interaction region or if no energy is released in the calorimeters. A positive decision at this level triggers the recording of the data.

From the front-end electronics and onto the recording, the flow of data is controlled by the Data Acquisition System (DAS). Upon a positive T2 decision, the DAS transfers the data from FEBs to the Multi-Event Buffer (MEB). T3 decision enables the Global Event Supervisor (GES) software to transfer the data to the Global Event Buffer (GEB) and to build a full ZEBRA [22] structure of the event. The event is then transferred and recorded pending the decision of T4. For a typical luminosity of $1.5 \times 10^{31}\ cm^{-2}s^{-1}$, T1 reduces the event rate from 90 kHz to $\sim$ 800 Hz. T2 further reduces the rate to $\sim$ 5 Hz. After T2, about 20% of the data contain physics events; the physics rate is composed of $\sim$ 0.5 Hz and $\sim$ 0.07 Hz of hadronic and leptonic Z^0 decays, respectively, and $\sim$ 0.5 Hz of Bhabha events. With the rejection rate of 1.5 Hz for each of the two final stage triggers, the recording rate at DELPHI is about 2 Hz.

After four levels of successive triggers to identify interesting events, about 55% of the recorded events are background events resulting mainly from beam–gas interactions, synchrotron radiation and cosmic ray events. Approximately 15% Z decays and 30% Bhabha events comprise the recorded events. Of the Z decay events, leptonic and hadronic events can be separated by examining the final state multiplicity. The trigger efficiency for hadronic Z events, because of their large multiplicity of charged tracks, is consistent with 1. For the leptonic events with their simple two-track topology, except in the case of τ events, the trigger efficiency is also close to 1.

4 PREPARATION

As discussed in Chapter 1, the analysis follows the charge correlation method. By correlating the sign of the charge of the lepton to that of the b-quark in the decaying b-hadron, one can determine whether the lepton is a primary or secondary decay product of the b-hadron. The charge of the lepton can be easily obtained from the direction of the track curvature. Obtaining the charge of the b-quark, however, is not a trivial task. To do this, the b-hadrons must be reconstructed in the events. For each reconstructed b-hadron, then, an attempt is made to identify whether a b- or $\bar{b}$-quark composes the b-hadron. A series of neural network algorithms is employed to accomplish the identification process. In addition to these techniques, in order to understand the data taken by DELPHI, a simulation sample needs to be prepared. The simulated data are then compared to the real data to help study the background and to model the signals to be measured.

4.1 Event selection

During the data taking periods at DELPHI in 1994 and 1995, over nine million events were collected for further analyses. As discussed in Section 3.2.1, there are many types of events. Out of the nine million events, only about two million events are expected to be of hadronic type. A further reduction is made when isolating b-quark hemispheres. In addition, the physical conditions of the critical subdetectors constrain the total number of events used in the analysis. A good example is the con-

dition of the RICH detector, as the particle identification plays an important role in determining the charge of the b-quark. The RICH detector, unfortunately, was fully operational only for half the data–taking period in 1995. The details of the selection and the number of events that pass each cut are presented in the following subsections.

4.1.1 Preselection

Before applying more sophisticated algorithms for selecting the events to be used in the analysis, a standard method of eliminating background and non-hadronic events is applied. From the different types of events described in Section 3.2.1, hadronic events, consistent with $Z^0 \rightarrow q\bar{q}$, can be selected by imposing for each event the following requirements:

- total energy of the charged particles $> 0.15 E_{CM}$
- at least seven charged particles.

These requirements eliminate low multiplicity $Z \rightarrow e^+e^-$ and $Z \rightarrow \mu^+\mu^-$ events and reduce the background, mainly from $\tau^+\tau^-$ pairs, $\gamma\gamma$ collisions, cosmic and beam-gas events. In the above and throughout the analysis, a charged particle is considered only if it meets the following requirements:

- the polar angle is between $20° < \theta < 160°$
- the track length is larger than 30 cm
- impact parameter relative to the nominal beam spot is less than 5 cm in the $r\phi$ plane and 10 cm along the beam direction
- the momentum is larger than 200 MeV/c and the relative uncertainty smaller than 100 %.

Neutral particles with larger than 500 MeV of energy measured by the HPC and the hadronic calorimeters are considered. From these requirements, 2,033,080 events are selected as hadronic events.

Since the analysis is performed for electrons and muons separately, different detector requirements for each lepton type are imposed. For the electron analysis, VD, TPC and HPC are required to be in perfect working condition, whereas the muon analysis requires VD, TPC and MUB to be in perfect working order. From the selected hadronic events, 1,876,346 events satisfy the detector requirements for the electron analysis, and 1,757,309 events meet the requirements for the muon analysis.

In addition, the event thrust axis is limited to the barrel region: $|cos\ \theta_{thrust}| < 0.75$. This requirement virtually eliminates the background from $\gamma\gamma$ process. These requirements lead to an efficiency of selecting hadronic events to be about 95 % while all background sources are found in less than 0.1 % of the cases. The total number of hadronic events selected for the electron analysis is 1,376,385 and for the muon analysis is 1,288,825.

In the selected hadronic barrel events, b-tagging is performed for each hemisphere. 329,859 and 308,599 hemispheres satisfy the b-tagging requirements in the electron and muon analyses, respectively. Further reduction is made when requiring perfect RICH for the optimal b-quark charge determination. After satisfying all these requirements, the final number of hemispheres to be analyzed is 254,147 for the electron analysis and 249,280 for the muon analysis. Table 4.1 lists these initial selections for each year.

4.1.2 Enhancing b-quark events

The process of selecting b-quark events is referred to as b-tagging. b-tagging takes advantage of the long and measurable lifetimes of b-hadrons. This process, however,

Table 4.1 Initial selection results

Criteria	Number of selections made			
	1994		1995	
	$e^{\pm}$ analysis	$\mu^{\pm}$ analysis	$e^{\pm}$ analysis	$\mu^{\pm}$ analysis
Total events	5,753,343		3,661,917	
Hadronic events	1,370,203		662,877	
Perfect detector condition	1,228,789	1,204,830	647,557	552,479
Barrel events	903,135	884,945	473,250	403,880
b-tagged hemispheres	216,891	212,684	112,968	95,915
Above with perfect RICH	188,658	192,101	65,489	57,179

presents a bias toward selecting the b-hadrons with longer lifetimes. To avoid such a bias, each event is divided into two hemispheres with respect to the thrust axis as described in Section 3.2.1, and the b-tagging is applied to each hemisphere separately. Then, the hemisphere opposite to the b-tagged hemisphere is selected for the analysis. This method avoids introducing a bias on the relative fraction of the different b-hadron species selected for the analysis.

The b-tagging technique employed by this analysis takes advantage of several characteristics displayed only in b-quark events. For each hemisphere, the particles are clustered into a jet or jets using the JADE [23] algorithm, and an attempt to reconstruct the secondary vertex is made. If the secondary vertex is successfully reconstructed, a single variable is assigned to represent a b-tagging probability, which combine four determining characteristics: the effective mass of the secondary vertex, the rapidity of the particles included in the secondary vertex, the fraction of the energy of the jet carried by charged particles, and the jet lifetime probability. This technique has been successfully used in the measurement of the relative decay width of the Z^0 into b-quarks or $R_b = \Gamma_{b\bar{b}}/\Gamma_{had}$ [24].

The purity of the b-tagging technique can be calculated by using

$$N_b^H = N_{tag}^H - 2N_{had}(\varepsilon_c \cdot R_c + \varepsilon_{uds} \cdot R_{uds}), \tag{4.1}$$

where $R_{uds} = 1 - R_b - R_c$, R_b and R_c are the LEP averages taken from [25], and the efficiencies ε_c and ε_{uds} are estimated from the simulation studies. Table 4.2 shows the exact input values including ε_b, which is not used in the calculation above but listed as a reference. The purity and the corresponding efficiency resulting from this b-tagging technique is shown in Figure 4.1. A value for the b-tagging variable is chosen as to give 92.6±0.3(stat.)% purity for the selected hemispheres.

4.2 b-hadron charge determination

The process by which the charge of the b-quark is determined is by examining the decay properties of the b-hadron. This requires a full reconstruction of the weakly decaying b-hadron and the ability to distinguish the tracks originated from the decay of b-hadron from those originated from the fragmentation. The b-tracks are then used to reconstruct the decays of b-hadrons. After reconstructing b-hadrons, the properties of the reconstructed b-hadrons and their decay products are used to determine the charges of the b-quarks in the decayed b-hadrons. This process is performed for each hemisphere independently. Special care is taken as to not contaminate the output of the process by combining the information from both hemispheres in the event. If the properties of both hemispheres were to be combined, the estimated charge for one side affects the determination of the charge on the opposite side. Our approach masks the influence of neutral b-meson mixing in the measurement process.

Table 4.2 Input parameters for b-purity calculation

input variable	value
ε_b	$(42.50 \pm 0.06(\text{stat}))\%$
ε_c	$(3.01 \pm 0.02(\text{stat}))\%$
ε_{uds}	$(0.329 \pm 0.003(\text{stat}))\%$
R_b	0.2170 ± 0.0009
R_c	0.1734 ± 0.0048

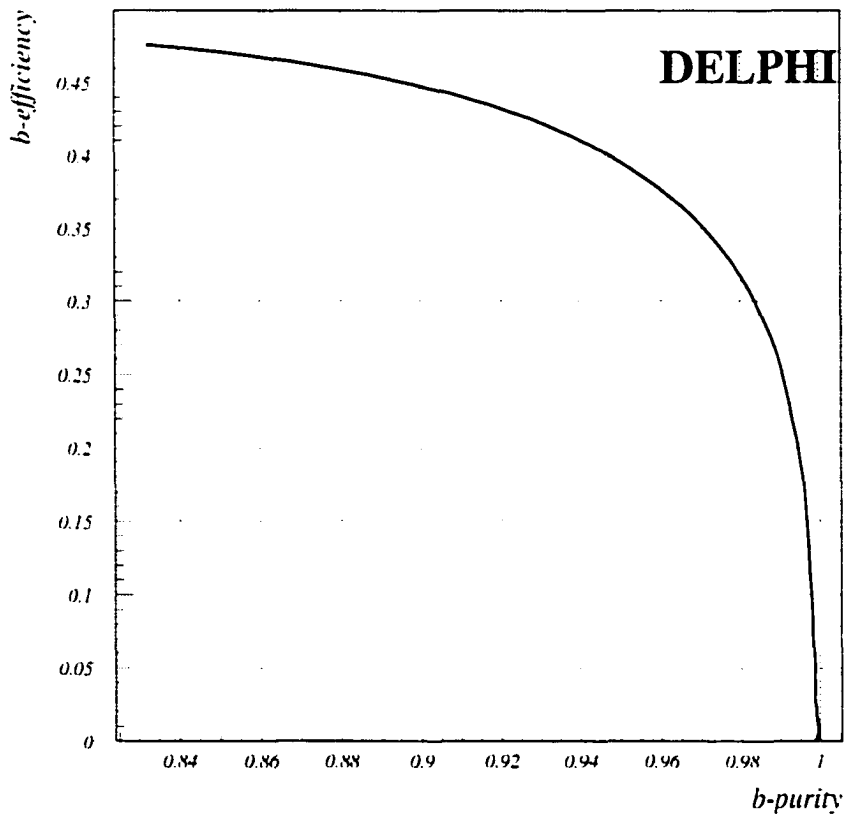

Figure 4.1 Efficiency versus purity is shown for the b-tagging technique.

4.2.1 Reconstruction of b-hadrons

The reconstruction of the weakly decaying b-hadrons starts with identifying event jets. In clustering, each track is considered a cluster and the tracks with the transverse momentum of less than 5 GeV/c with respect to the closest cluster are joined as a jet. For events with two jets, the jet axis in each hemisphere is used as the reference axis for the rapidity calculation. If more than two jets are found in the event, the jet with the highest energy in the hemisphere is chosen as the reference axis. The rapidity of each track is then calculated along the reference axis:

$$y = \frac{1}{2} ln(\frac{E + P_L}{E - P_L}), \tag{4.2}$$

where E is the energy, and P_L is the longitudinal momentum along the reference axis of the track. Simulation studies indicate that the rapidity of the b-tracks tend to lie outside the central rapidity window of $-1.6 < y < 1.6$, as shown in Figure 4.2.

The next stage is to reconstruct the b-hadrons using the tracks with the rapidity $|y| > 1.6$. By summing up the track momenta, an initial estimate of the b-hadron four-vector is made. However, the cut imposed on the value of the rapidity excludes some b-tracks. This, along with tracks that are lost in the detector cracks, lowers the reconstructed b-hadron energy. Understanding the sources of the lower reconstructed energy presents the means to control it. The reconstructed mass of b-hadron helps to determine any eliminated b-tracks in the rapidity cut. Also, the total reconstructed energy in the hemisphere signals any lost tracks in the detector cracks. As these conditions can be simulated, a correction function is derived from simulation studies to adjust the initial estimate of the b-hadron energy. The adjusted b-hadron energy is compared to the actual energy generated in the simulation in Figure 4.3. The energy resolution from this technique is 7% for 75% of the b-hadrons.

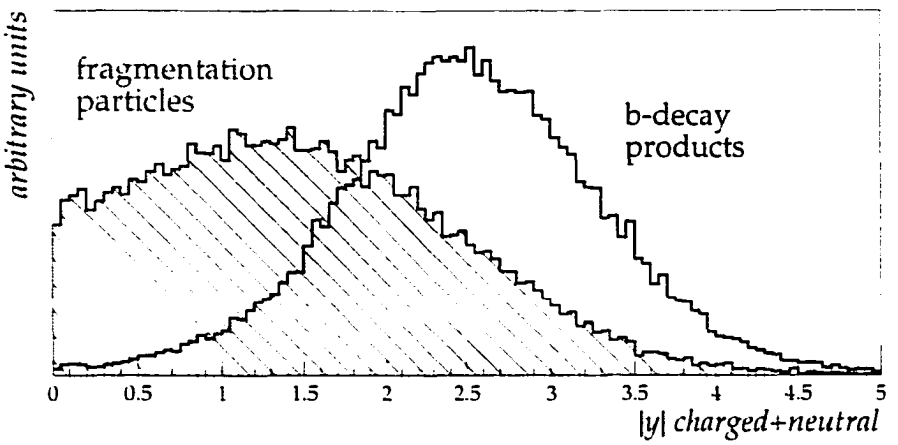

Figure 4.2 Comparison of rapidity distribution, $|y|$, for b-tracks and fragmentation tracks in simulated $b\bar{b}$ events

4.2.2 Charge determination

The determination of whether a b- or $\bar{b}$-quark comprises the decaying b-hadron starts with the fitting of a secondary vertex in each hemisphere. Using the event primary vertex as the starting point and the obtained b-hadron momentum as a directional constraint, the secondary vertex fit in three dimensions is performed. The tracks with the rapidity $|y| > 1.6$ are used at the start. If the fit does not converge, the track with the highest contribution to the χ^2 is taken out, and the fit is repeated. A successful fit yields, along with the position of the secondary vertex, the updated position of the primary vertex and the updated direction of the b-hadron to correspond to the fitted vertices. The decay length of the b-hadron can also be estimated as the distance between the primary and the secondary vertices.

Once the secondary vertex is established, b-tracks are distinguished from the fragmentation tracks by using a neural network. The charges of the b-tracks selected from this process are added to provide an estimate of the decayed b-hadron charge. The estimated b-hadron charge is then combined with other hemisphere information to finally estimate the charge of the b-quark in the decayed b-hadron. Since the use of

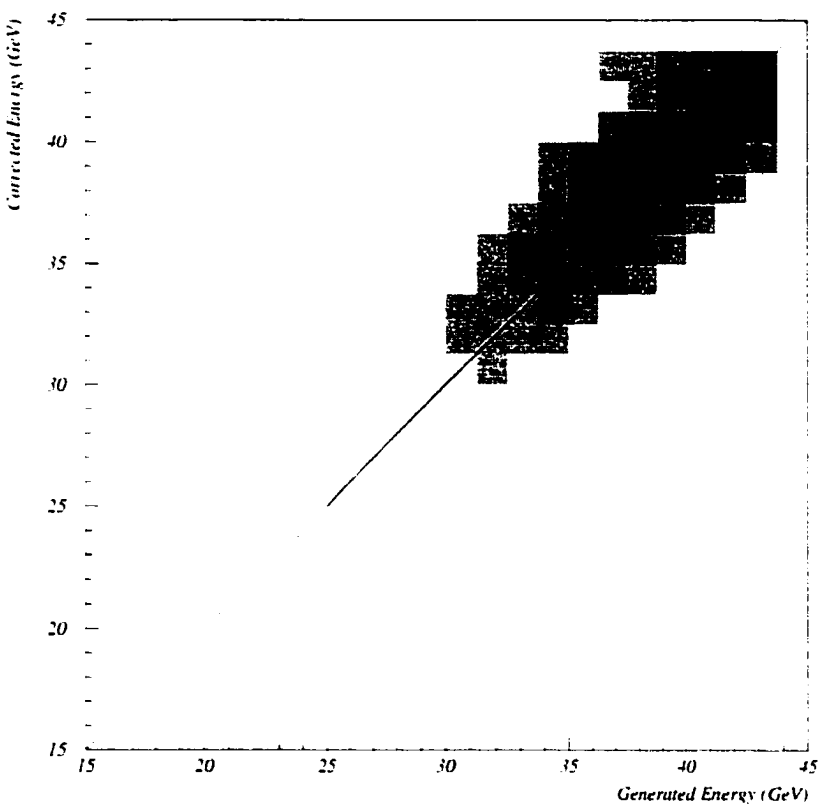

Figure 4.3 b-hadron energy after reconstruction is compared with the true b-hadron energy generated in simulation. Darker blocks represent more data points.

neural network algorithm is at the heart of the determination process, a brief description of the workings of neural network is first presented. The details of the process of determining the charge of the b-quark in the decayed b-hadron then follow.

4.2.2.1 Neural network algorithm

The ability to sort out the complex dependencies of multiple parameters to a binary answer lies at the heart of any neural network algorithm. The application of neural network to the difficult question of whether a b- or $\bar{b}$-quark comprises the decayed b-hadron is only natural, as the combination of several factors helps to determine the answer. The success and the performance of neural network depend on the parameters given to the network.

The neural network scheme employed to accomplish the task is JETNET [26]. The internal structure of the neural network is divided into three layers: input, hidden and output layers. Each layer is composed of a number of nodes. Each input node contains one input variable to the network and is connected to all the nodes in the next layer with the weight of w_{ij}. In the training process, the weights, represented by lines connecting the nodes in Figure 4.4, are calculated by using a set of predetermined outputs. The calculation of the weights is done by parameterizing the nodes of one layer to the nodes of the next layer—from input nodes to hidden nodes and from hidden nodes to the output node. This forward training method classifies the employed neural network as feed-forward neural network.

4.2.2.2 Stage 1: fragmentation or b-track?

The first application of the neural network algorithm is to determine whether a track originates from the primary vertex or the fitted secondary vertex. The tracks with higher probability of originating from the secondary vertex are considered to be

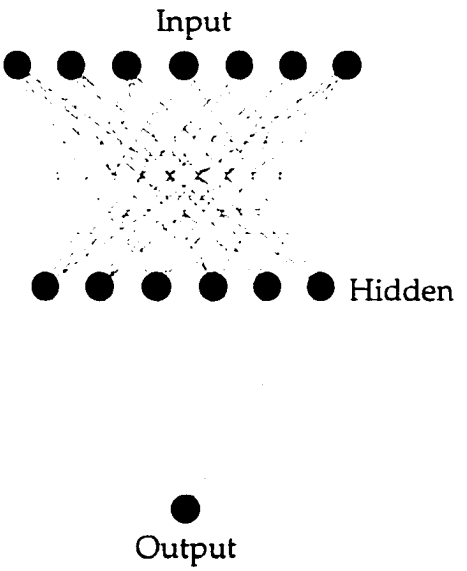

Figure 4.4 A schematic view of a three-layer neural network

b-hadron decay products. The rapidity method does separate most tracks according to their origins; however, the separation is not adequate to establish the charges of the b-hadrons.

The choice of the input parameters to the neural network is critical to the success of this method. In this case, the input variables start with the track rapidity. As discussed above, the b-hadron decay products have higher rapidity, $|y|$, than fragmentation particles. Next is the information obtained while fitting the secondary vertex. Each track is assigned probabilities for originating from the primary vertex and the secondary vertex. These probabilities, as the b-hadron decay products are expected to have higher probability to originate from the secondary vertex and lower for the primary vertex, are also included as discriminating input variables. The laboratory momentum of the track is the next input variable. Because of the hard fragmentation of b-quarks, the b-hadron decay products tend to have higher laboratory momenta than others. The momentum and the angle of the track in the b-hadron rest frame are also included. The momenta of fragmentation particles tend not to obey the energy

conservation in the b-hadron rest frame, and the angles in the b-hadron rest frame for the fragmentation particles point backwards.

More obvious choices are the information pertaining to the hemisphere since the absence of b-hadron signature must lead to non-selection of b-hadron decay products in that hemisphere. The input variable pertaining to this is the decay length, as described in Section 4.2.2, in the $r\phi$ plane. The discriminating power of some of these input variables are shown in Figure 4.5. The performance of this neural network is shown in Figure 4.6 in a logarithmic scale. The tracks with the output of the neural network, P_i, greater than 0.5 are used as b-hadron decay products in the fitting procedure.

4.2.2.3 Stage 2: b- or $\bar{b}$-quark?

After the first stage of neural network to separate the b-tracks from the fragmentation tracks, the electric charge of the reconstructed b-hadron can be estimated for each hemisphere. The charge is estimated by using all the tracks in the hemisphere

$$Q_{H_b} = \sum_{i\text{-th track}} Q_i P_i, \tag{4.3}$$

where Q_i and P_i are the charge and the output of the first stage of neural network of the i-th track. The error on this charge is calculated as

$$\sigma_{Q_{H_b}} = \sqrt{\sum P_i(1-P_i)}. \tag{4.4}$$

The distribution of the estimated b-hadron charge is shown in Figure 4.7. Already at this point, for a good number of charged b-hadrons, the charges of b-quarks can be extracted. As such, the calculated estimated charge and its error are the first input parameters to the second stage of neural network to determine the charge of the b-quark in a decaying b-hadron.

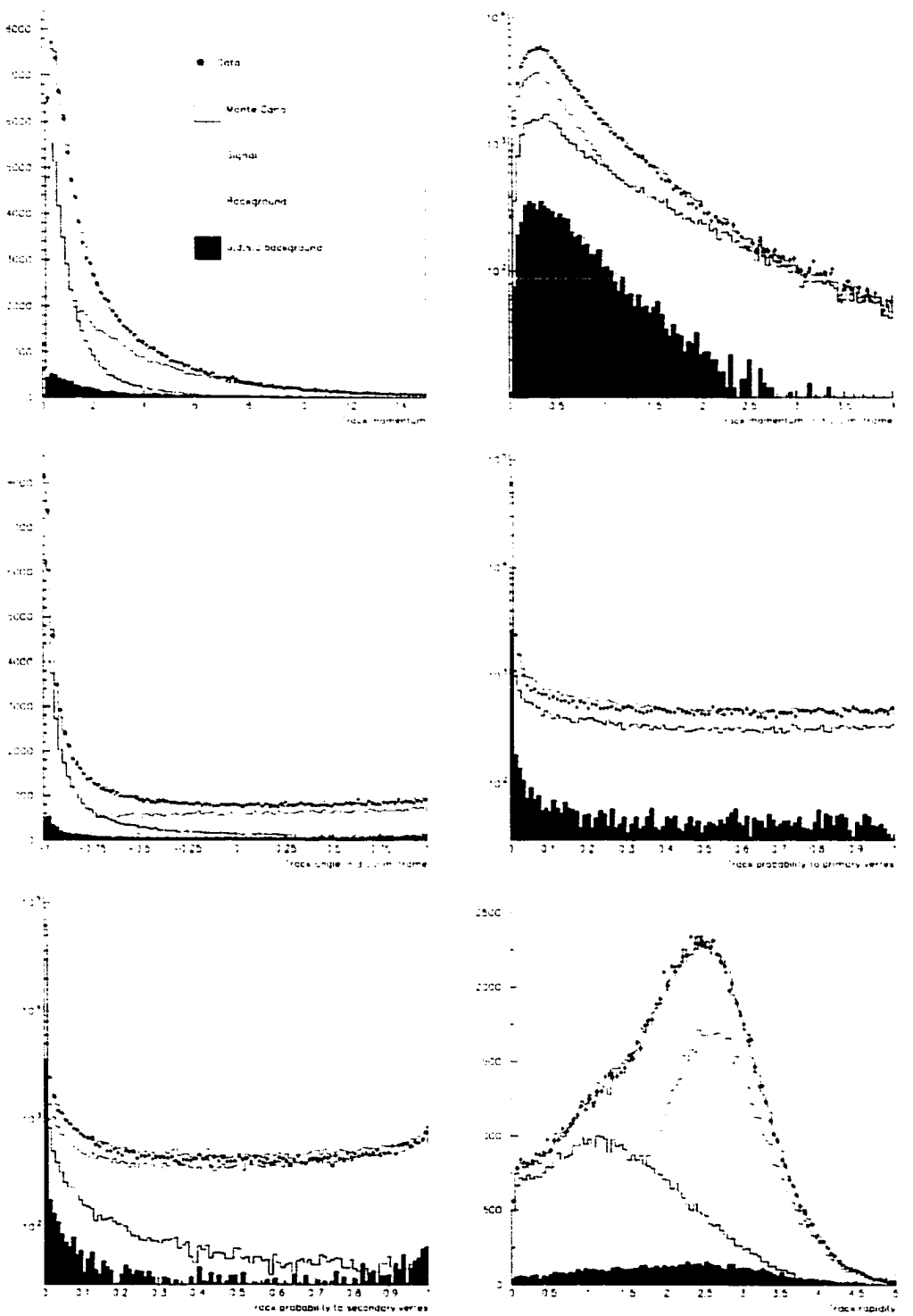

Figure 4.5 Distribution of input variables used in neural network to separate b decay products from fragmentation particles. Adapted from [27].

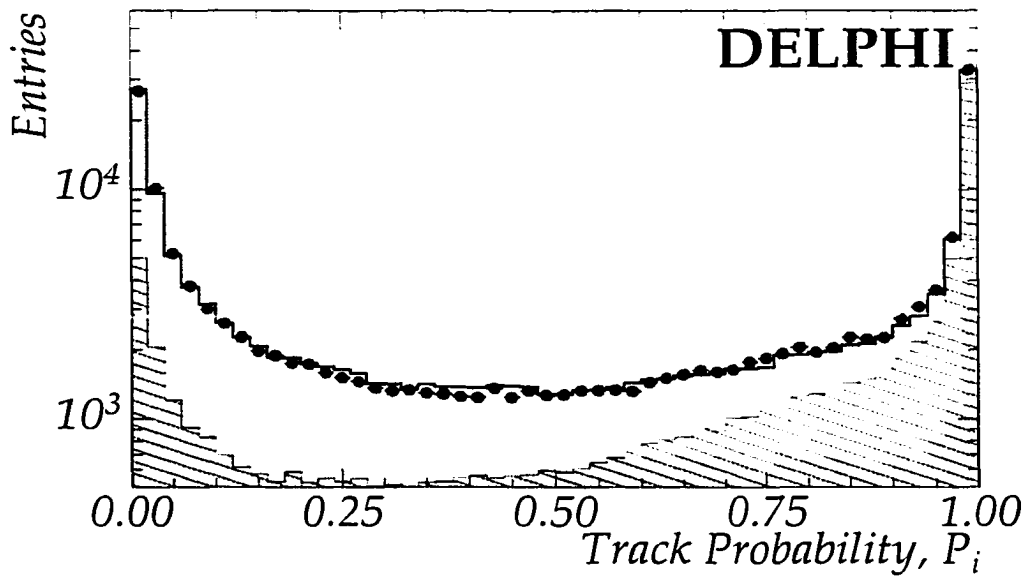

Figure 4.6 Output of the neural network comparing the distributions of real data (points) and the simulated data (histogram). For the simulated sample, fragmentation tracks are shown in shaded area and the b-tracks are shown in hatched area.

In addition to the estimated charge, the jet charge can be calculated and used as the next input parameter. The jet charge is defined as

$$Q_{jet} = \frac{\sum_i Q_i |P_L|_i^\kappa}{\sum_i |P_L|_i^\kappa}, \tag{4.5}$$

where P_L is the longitudinal momentum component of the i-th track with respect to the thrust axis, and κ is a free parameter. Following simulation studies, the optimal value of κ is determined to be 0.6. Next are the charge and momentum of the kaon track with the highest value of P_i. Kaon hypothesis is obtained from the procedure described in Section 3.2.3. As the charge of the b-hadron is carried by the kaon at a large rate, finding the kaon is an important ingredient which requires a perfectly performing RICH. Another clue comes from a slow pion. The decay of $D^{*+} \to D\pi^+$ has a very small Q-value with generally large D^* momentum and small pion momentum in the b-hadron rest frame. The charge of the pion can, therefore, be used to tag the charge of the b-hadron. With these input parameters, the output of the second stage

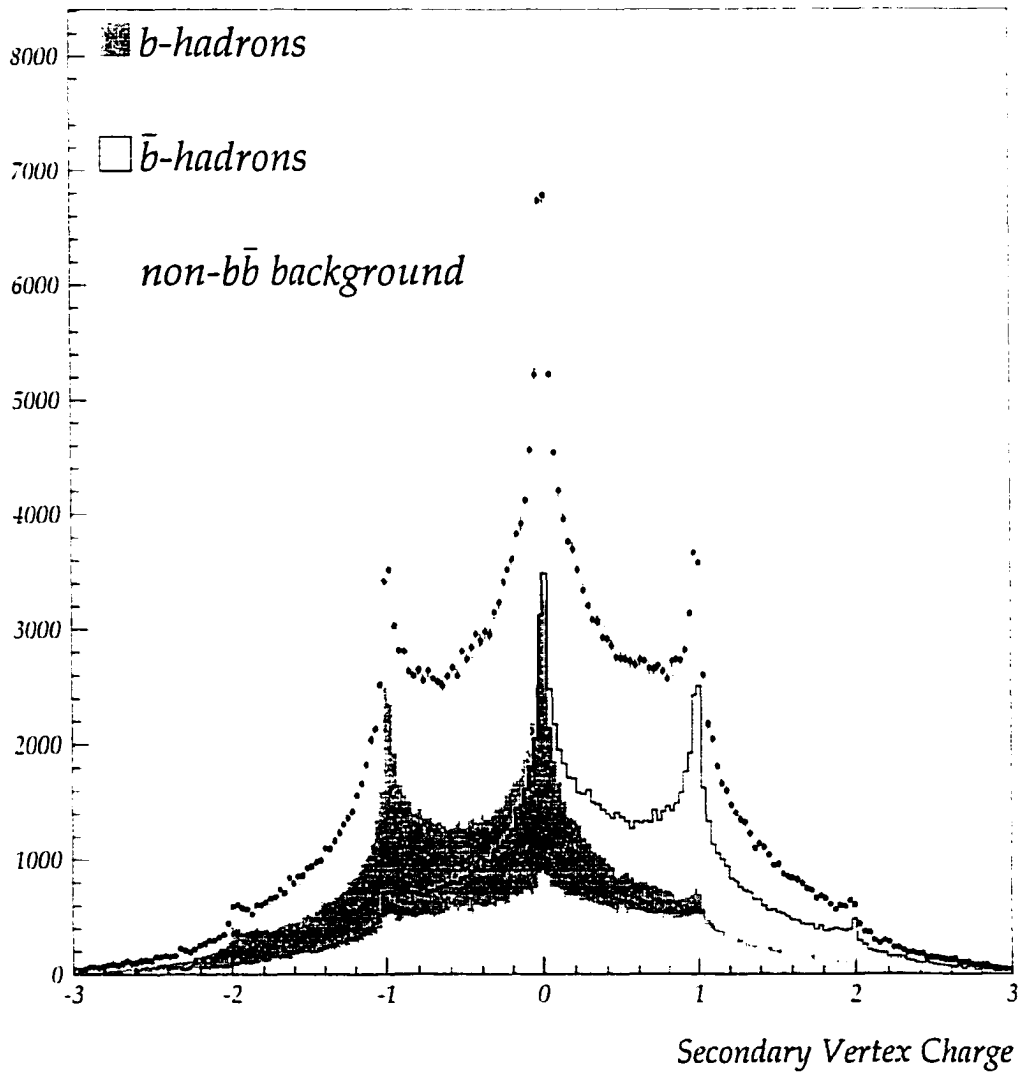

Figure 4.7 Estimated electric charge of b-hadron. The real data (points) are compared to the simulated data (solid line). For the simulation data, actual charges of the b-hadrons are shown.

of neural network is shown in Figure 4.8. The output, though not perfect, is used to classify b-hadrons. A b-hadron with the output of greater than 0.0 is assumed to contain a $\bar{b}$-quark, whereas the opposite is assumed for a b-hadron with the output of less than 0.0.

4.3 Simulation data

To interpret the real data taken by DELPHI, another set of data that are simulated with all the knowledge about the physics of collision, the following decay processes and the interactions with the detector material is required. The simulated data, if all the ingredients are complete and correct, should be the same as the real data. Any deviation indicates missing ingredients and/or incorrect knowledge. In this analysis, the data from simulations are used extensively to study the background and to obtain the momentum shapes of the leptonic decay modes. In what follows, the process of obtaining simulation data is briefly described. The topics of particular interest to this analysis, such as the comparison between the simulated leptons and the real ones and the upper–vertex simulation, are explained further.

4.3.1 Simulation

The complete simulation of the DELPHI data is conducted in two stages. The first stage is the generation of the e^+e^- collision and the subsequent decay of the intermediate Z^0. The second stage is the simulation of the processes that occur between the generated tracks and the components of the DELPHI detector. After the two stages, the simulated data have the same format as the real data taken by DELPHI. The two sets of data are then treated in the same manner in the analysis. The only difference for the simulated data is that the identity and the complete source of each track is known.

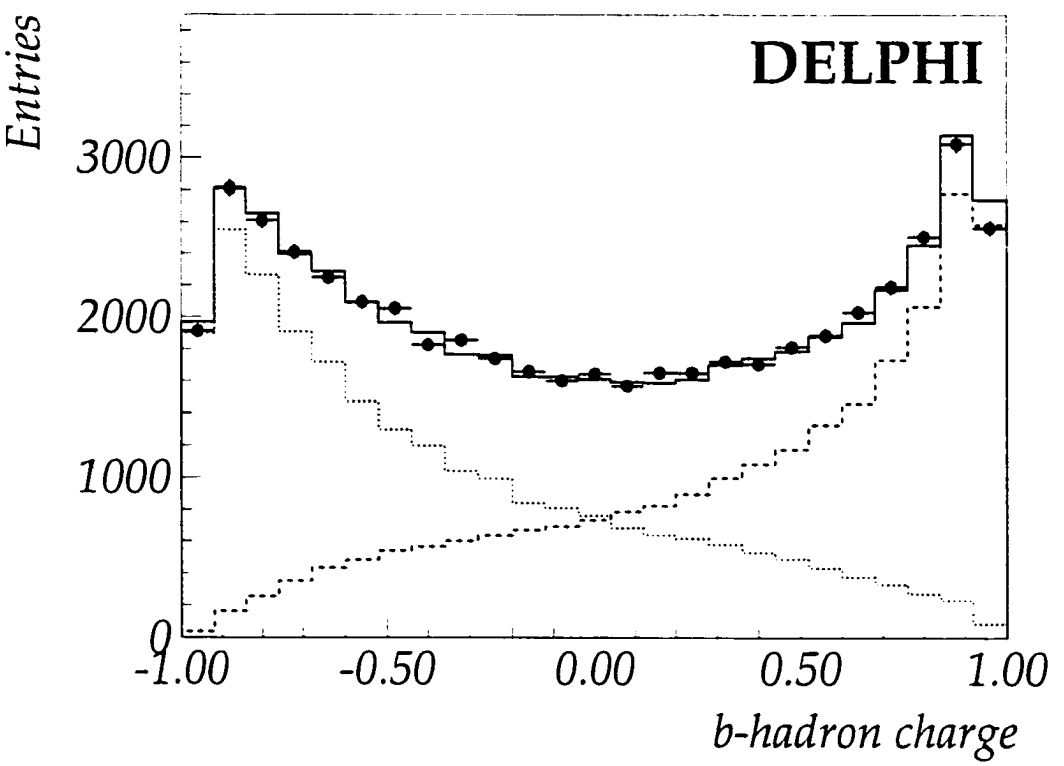

Figure 4.8 Output of neural network comparing the real (points) and simulated (solid histogram) data. For the simulation data, b-hadrons are shown as the dotted histogram, and $\bar{b}$-hadrons are shown as the dashed histogram.

The first stage of generating the collision and the subsequent hadronic decays is handled by the JETSET generator [28], which employs parton shower and string fragmentation in the $Z^0 \rightarrow q\bar{q}$ events. The parameters for the event generator are fixed to emulate the hadronic distributions measured by DELPHI [19]. The next stage of the simulation starts as the particles enter the active detector components. Separate simulation modules are built for each detector component to mimic the response of a real subdetector.

As shown in Table 4.3, the total of about four million generated $Z^0 \rightarrow q\bar{q}$ events are used in this analysis. Most of the generated events pass the hadronic requirements. Requiring barrel events, as done for the real data described in Section 4.1.1, reduces the total to about three million events. The tagging of b-hadron hemispheres, as described in Section 4.1.2, selects about 700,000 hemispheres.

4.3.2 Leptonic spectra

In the semileptonic decays of b-hadrons, the ISGW model is used to simulate the momentum spectra of electrons and muons. A simple reweighting procedure for the spectra is developed to provide spectra for other models considered, such as ACCMM and a modified ISGW. The modified ISGW, or ISGW**, enhances the contribution of the excited charmed state, D^{**}, from 11% to 32% to better align with the results from CLEO. Following the prescription of the LEP Electroweak Working Group (LEP-

Table 4.3 Number of simulated events

	1994	1995
Total events	3,270,401	1,125651
Hadronic events	3,083,376	1,062,299
Barrel events	2,263,516	776,525
b-tagged hemispheres	527,777	178,829

EWWG) [25], the parameters for the ACCMM model are set to $p_f = 298\text{MeV}/c$ and $m_c = 1673\text{MeV}/c^2$, also to follow the results from CLEO. Figure 4.9 compares the momentum spectra of the three models.

For the secondary leptons in the process $b \to c \to \ell$, two separate processes: $b \to D$ and $c \to \ell$ need to be modelled. The D momentum distribution is modelled using the results from CLEO. The measurements from other lower energy experiments, DELCO and MARK III, are used to parametrize the $c \to \ell$ decay following the ACCMM model. The parameters established by the LEPEWWG for the ACCMM model are $m_s = 0.001 \pm 0.152\text{GeV}/c^2$ and $p_f = 0.467^{+0.205}_{-0.114}\text{GeV}/c$. Covering the full range of these parameters, three spectra are suggested by the LEPEWWG. The parameters for each spectrum are listed in Table 4.4, and the three spectra are shown in Figure 4.10.

4.3.3 Simulated leptons versus real leptons

The studies of efficiency and misidentification probability are conducted for the simulated leptons in the same manner described for real leptons in Sections 3.2.4.2 and 3.2.5.2. Differences in efficiencies and misidentification probabilities are found between the leptons in the real data and the ones in the simulated data. The leptons in the simulated data, therefore, need to be rescaled to match the efficiencies and misidentification probabilities of the real leptons. The ratios used to rescale the simulated leptons are listed in Table 4.5. The muon efficiencies for both types of data agree within a precision of 1.5% and therefore are not listed.

Table 4.4 Parameters used for calculation of $b \to c \to \ell$ models

	m_s (GeV/c^2)	p_f (GeV/c)
ACCMM1	0.001	0.467
ACCMM2	0.001	0.353
ACCMM3	0.153	0.467

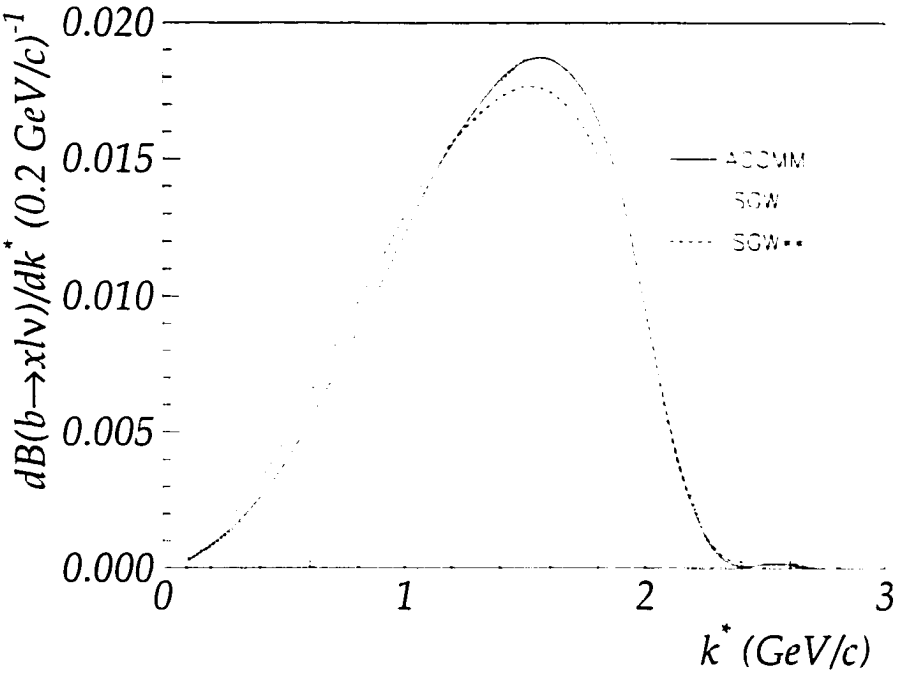

Figure 4.9 The momentum spectra for the process $b \to \ell$ for different models are shown. ACCMM, ISGW and ISGW** are shown as solid, dotted and dashed lines respectively.

Table 4.5 Applied ratios of efficiencies and misidentification probabilities to simulated leptons.

	1994	1995
e efficiency	0.92 ± 0.02	0.93 ± 0.02
e misidentification	0.76 ± 0.05	0.70 ± 0.06
μ misidentification	2.03 ± 0.12	1.22 ± 0.20

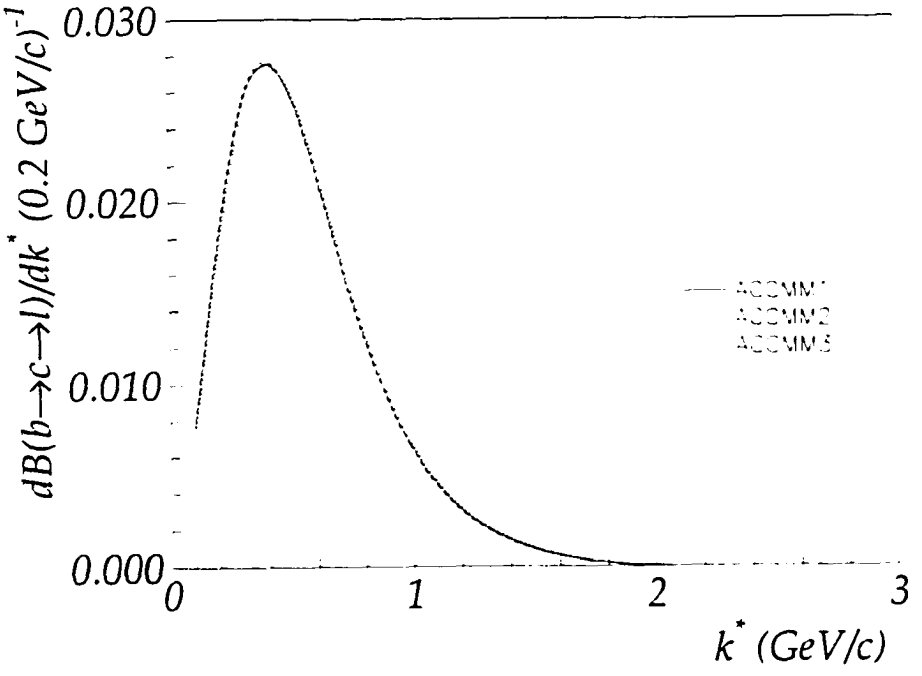

Figure 4.10 The momentum spectra for the process $b \to c \to \ell$ for different models are shown. ACCMM1, ACCMM2 and ACCMM3 are shown as solid, dotted and dashed lines respectively.

4.3.4 Upper–vertex simulation

Much of the information on the upper vertex has been obtained in the recent years, as the new related measurements become available. It is now assumed that the probability of obtaining a different species of c-hadron from the W or the upper vertex is independent of the nature of the decaying b-hadron. As such, the measurements of different upper–vertex c-hadron species are taken into account and combined with $c \to \ell$ model to provide the leptonic spectrum. By using the rates of $H_b \to DDX$ measured by ALEPH and the rates of flavor specific $B \to D$ measurements by CLEO, the LEPEWWG suggests the branching fraction for the upper–vertex leptons to be

$$\mathrm{BR}(b \to \bar{c} \to \ell) = 0.0162^{+0.0044}_{-0.0036}, \tag{4.6}$$

where the individual contributions are

$$\mathrm{BR}(b \to W \to D^{0/+} \to \ell) = 0.0091^{+0.0027}_{-0.0026}$$

$$\mathrm{BR}(b \to W \to D_s \to \ell) = 0.0071^{+0.0035}_{-0.0025}$$

$$\mathrm{BR}(b \to W \to \Lambda_c^+ \to \ell) = 0.0002^{+0.0001}_{-0.0002}.$$

The momentum spectrum for the upper–vertex leptons with individual spectrum for each decay mode is shown in Figure 4.11.

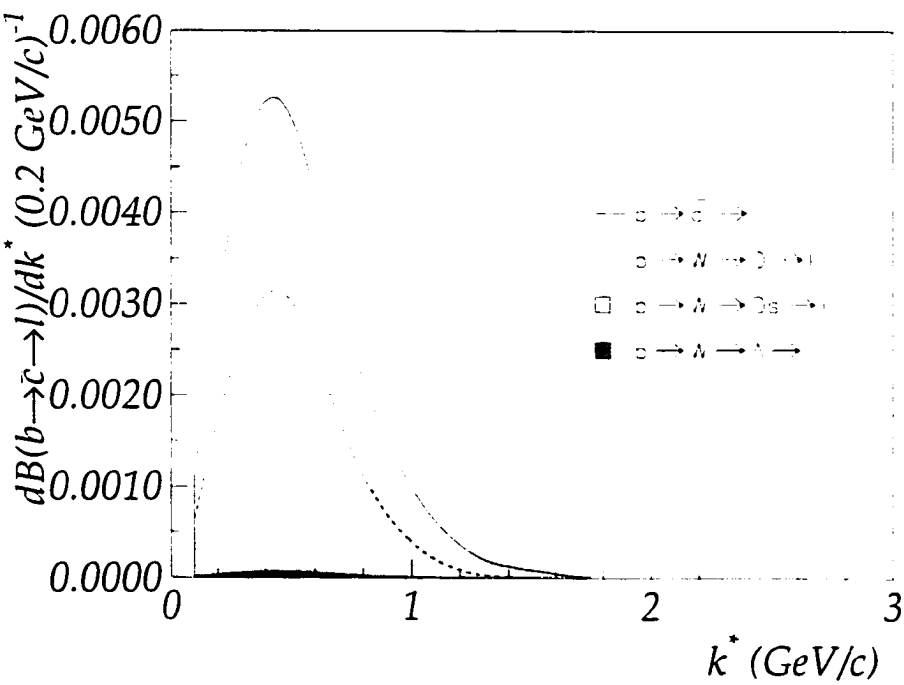

Figure 4.11 Momentum spectra for different modes of the upper–vertex leptons.

5 RESULTS

In the selected hemispheres, enriched with the b-hadron decays by the means of b-tagging on the opposite side, b-hadrons are reconstructed; the charges of b-quarks are estimated; and the tracks are classified into either fragmentation or b-hadron decay products. The simulation data is also prepared to assist in the study of background. With all the preparation done, the task now turns to the actual measurement. The measurement requires two classes of selected leptons: same sign and opposite sign. The same–sign leptons have the same sign of electric charge as the b-quarks in the decayed b-hadrons and are composed of direct leptons, $b \rightarrow \ell$, and upper–vertex leptons, $b \rightarrow \bar{c} \rightarrow \ell$. The opposite–sign leptons are the secondary leptons created in the process $b \rightarrow c \rightarrow \ell$. From these classes, known backgrounds from simulation are subtracted.

The fitting procedure involves the simulated spectra of different leptonic decay modes. Since the simulated spectra are calculated in the rest frame of the decaying b-hadron, the laboratory momenta of leptons need to be translated to the momenta in the b-hadron rest frame. After the translation, each class of leptons is fitted with the expected signal spectra. The measurements are then obtained from the fitting procedure. The measurements at this point are not complete without scrutinizing the entire analysis. The resulting uncertainties are added to the measurements to provide the final results.

5.1 Lepton spectra and background

To separate the selected leptons into two classes, same sign and opposite sign, for each hemisphere, the charges of the leptons are compared to the sign of the electric charge of the b-quark in the decaying b-hadron. This provides the first level of separation between the direct leptons and the cascade leptons, as the same–sign class is comprised of the leptons from the $b \to \ell$ and $b \to \bar{c} \to \ell$ decay modes, and the cascade leptons in the process $b \to c \to \ell$ comprises the opposite–sign class. Then for the fitting purpose, the laboratory momentum of each lepton is boosted to the b-hadron rest frame. The four-momentum of the reconstructed b-hadron described in Section 4.2.1 is used to translate the lepton momentum. The resulting lepton momenta in the b-hadron rest frame, denoted by k^*, have an average resolution of $\sigma(k^*) = 0.1\ \mathrm{GeV}/c$. The comparison between the k^* reconstructed in this fashion and the actual k^* in the simulation is shown in Figure 5.1.

For electrons and muons, separate sets of two histograms are made using $Q'_b \cdot Q_{\ell(e,\mu)} \cdot k^*$, where Q'_b is the sign of the charge of the b-quark, -1 or $+1$, and Q_ℓ is the charge of the lepton. This divides the two classes, same and opposite sign, and each class is binned into k^*. The known background processes are then subtracted. The first background is the set of fake leptons. The hadrons, identified as leptons, are subtracted using the estimates from simulation. From the remaining leptons, the leptons of fragmentation origin and in non-$b\bar{b}$ events are also subtracted. The background processes, which contribute leptons, include

- $b \to \tau \to \ell$
- $b \to J/\psi \to \ell^+\ell^-$
- $c \to \ell$.

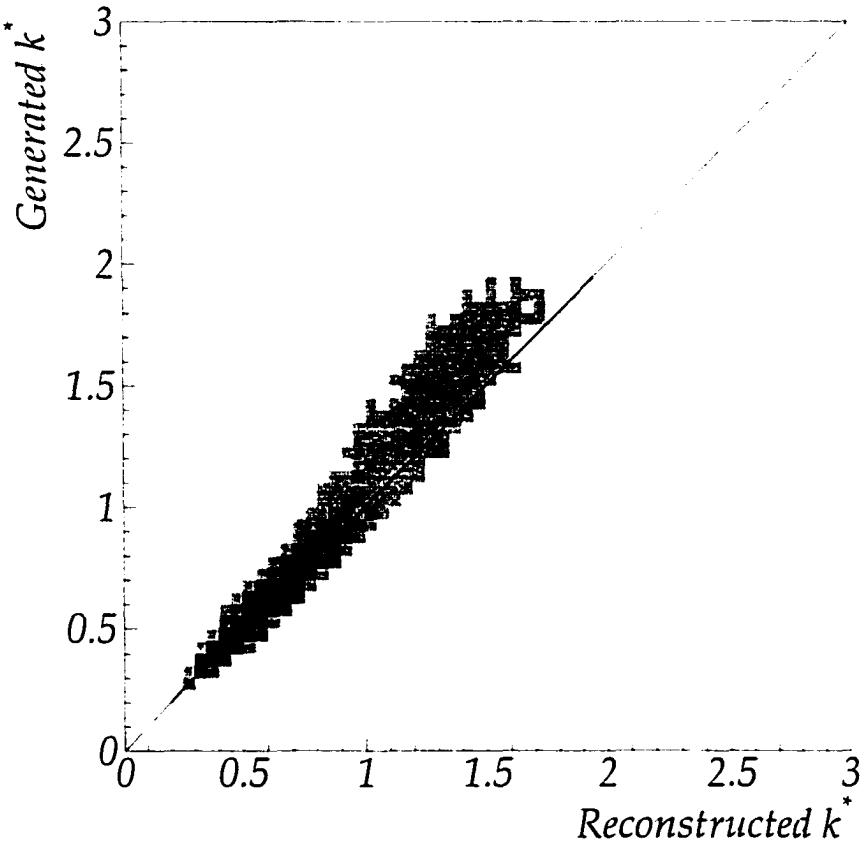

Figure 5.1 Comparison between the reconstructed k^* and the generated k^* in the simulation. Darker blocks represent more data points.

These processes are subtracted assuming the latest measured branching fractions [25]. The leptons found in rare events, such as $g \to c\bar{c}$ and $g \to b\bar{b}$, are subtracted as well. At this point, the remaining leptons are assumed to have originated from the desired decay modes.

5.2 Fitting and results

In classifying leptons into same sign and opposite sign, the charges of the b-quarks are used as assigned by the neural network described in Section 4.2.2.3. The simulation indicates, as shown in Figure 4.8, that these assigned charges are not exact, and wrongly assigned charges of b-quarks do exist. Because of this situation, some leptons are misclassified. Therefore, unlike the assumptions made about the composition of each class, both classes contain leptons from all three decay modes. Since having to rely on the simulation to predict the amount of misclassified leptons directly affects the measurements, a fitting procedure is developed to avoid relying heavily on the simulation.

Both classes are fitted by using binned χ^2 fit simultaneously starting with the amount of misclassified leptons assumed to the simulation expectation. For the same–sign spectra, the expected spectra of $b \to \ell, b \to \bar{c} \to \ell$ and of misclassified $b \to c \to \ell$ are fitted, while for the opposite sign, the spectra of $b \to c \to \ell$ and of misclassified $b \to \ell$ and $b \to \bar{c} \to \ell$ are used. The branching fractions of the signal spectra are continuously adjusted to minimize the χ^2 on both classes while adjusting the amount of corresponding misclassified leptons. The procedure yields consistent results for both electrons and muons with the χ^2 per degree of freedom around 1.0. The results of this procedure when using ACCMM model for $b \to \ell$ mode and ACCMM1 model for $b \to c \to \ell$ mode are listed in Table 5.1. The covariant matrix for the statistical uncertainties from the fitting procedure is shown in Table 5.2. The measurements

using ACCMM and ACCMM1 models are taken as the central values in accordance to the suggestion of the LEPEWWG [25]. The other models, ISGW and ISGW** for $b \to \ell$ and ACCMM2 and ACCMM3 for $b \to c \to \ell$, are used as uncertainties in the measurements. Table 5.3 lists the results from fitting with different models. Figures 5.2 and 5.3 show the results for fitting with different $b \to c \to \ell$ models and $b \to \ell$ models, respectively. In the plots shown, both electrons and muons are combined, and the simulation spectra are adjusted to reflect the measured branching fractions.

5.3 Systematics uncertainties

In determining the uncertainties in the measured values, there are two different types of uncertainties to consider in addition to the statistical ones. The first type involves the technique used in the measurement. Every aspect of the measuring technique is scrutinized. The resulting uncertainties make up a portion of the experimental uncertainties. The second is of the theoretical type. Since the measurements rely on the simulation to provide the background information, the uncertainties in the assumed branching fractions and the shapes of the background processes need to be included as systematics. Although most of the second type of uncertainties are considered theoretical, those resulting from the choice of semileptonic decay models are quoted separately to follow the guidelines of the LEPEWWG.

Table 5.1 Fitting results with statistical uncertainties

	1994	1995	combined
$\mathrm{BR}(b \to \ell)$ (%)	10.78±0.18	10.67±0.30	10.75±0.15
$\mathrm{BR}(b \to c \to \ell)$ (%)	8.02±0.31	7.92±0.52	7.99±0.27
$\mathrm{BR}(b \to \bar{c} \to \ell)$ (%)	1.33±0.32	1.36±0.50	1.34±0.30

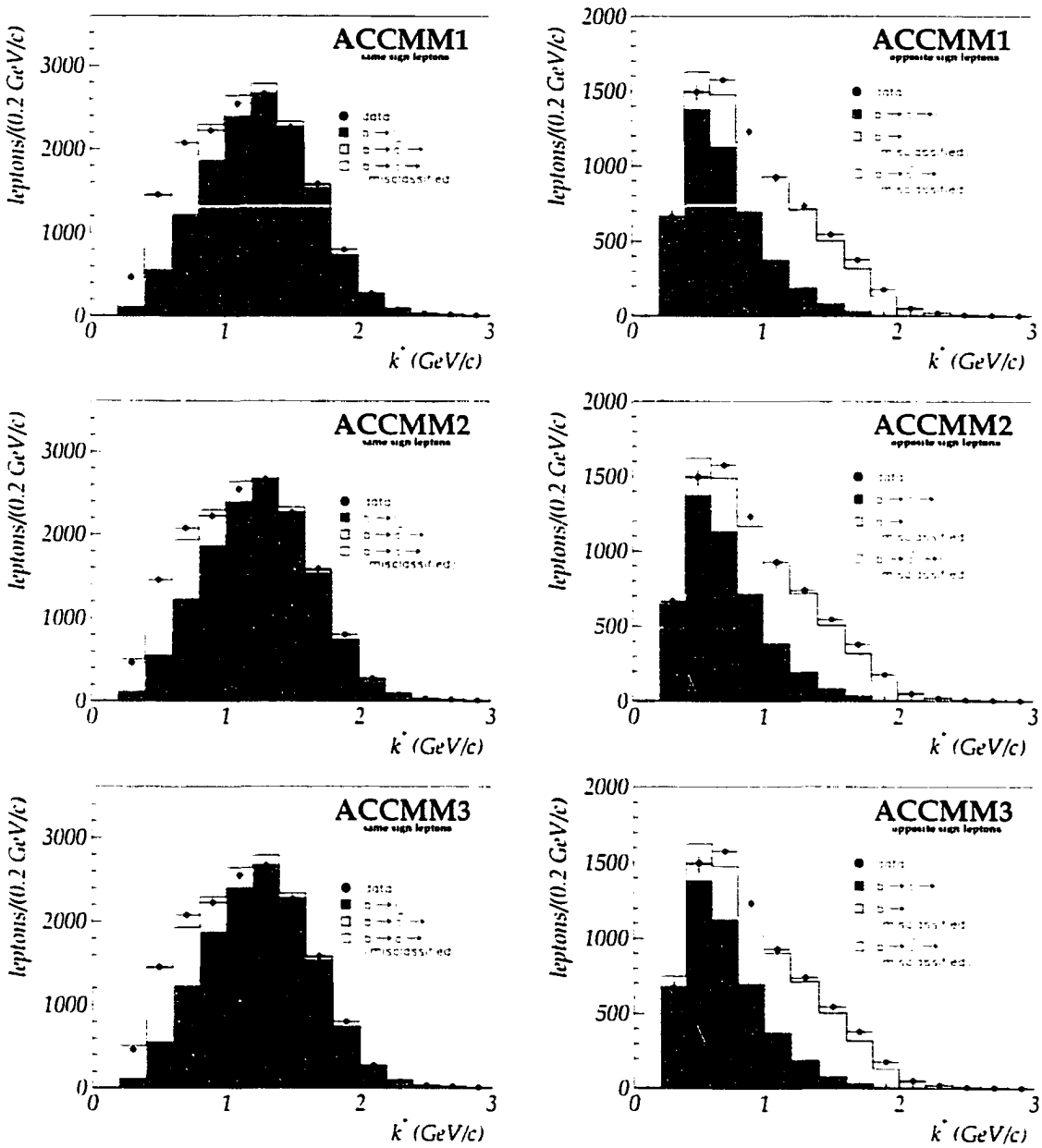

Figure 5.2 Fitting results for ACCMM $b \to \ell$ model and the three models of $b \to c \to \ell$ are shown. For the display purpose, the leptons are combined, and the simulation spectra are adjusted to correspond to the fitting results.

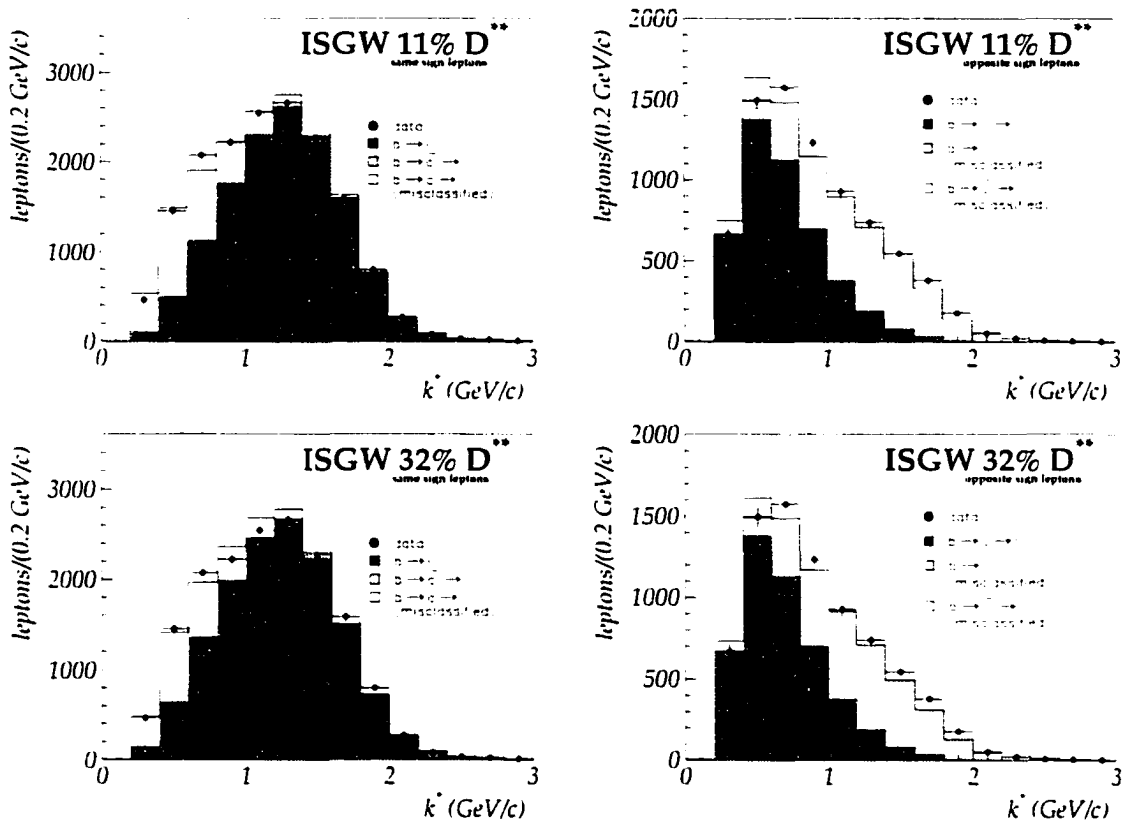

Figure 5.3 Fitting results for $b \to \ell$ models, ISGW and ISGW**, are shown with $b \to c \to \ell$ model set to ACCMM1. For the display purpose, the leptons are combined, and the simulation spectra are adjusted to correspond to the fitting results.

Table 5.2 Correlation matrix in the fitting

	$BR(b \to \ell)$	$BR(b \to c \to \ell)$	$BR(b \to \bar{c} \to \ell)$
$BR(b \to \ell)$	1.00	−0.077	−0.350
$BR(b \to c \to \ell)$		1.00	−0.603
$BR(b \to \bar{c} \to \ell)$			1.00

Table 5.3 Summary of results from the fitting procedure. The results are shown in percentages with statistical uncertainties.

$b \to \ell$ model	$b \to c \to \ell$ model	$b \to \ell$	$b \to \bar{c} \to \ell$	$b \to c \to \ell$
ACCMM	ACCMM1	10.75±0.15	1.34±0.30	7.99±0.27
ACCMM	ACCMM2	10.68±0.15	1.40±0.29	7.78±0.26
ACCMM	ACCMM3	10.82±0.16	1.29±0.30	8.08±0.26
ISGW	ACCMM1	10.53±0.14	1.70±0.32	8.03±0.26
ISGW**	ACCMM1	11.17±0.14	0.76±0.33	7.95±0.27

5.3.1 Experimental uncertainties

In examining the measuring techniques, some concerns are warranted in regards to the use and the possible correlation effects of the neural network algorithm. The uncertainties resulting from these concerns are considered first. The treatment of simulated leptons, as discussed in Section 4.3.3, is another concern, since the corrections to the simulated leptons contain statistical uncertainties. The technique of b-tagging also poses a concern, as the number of b-tagged hemisphere directly plays a role in the final measurements. Finally, the effects of having a finite simulated sample in the fitting procedure are addressed.

5.3.1.1 Neural network bias

Since the reconstruction and the charge tagging of the b-hadrons are done in the same hemisphere where the lepton selection is made, the correlation between the tagging of leptons and the charge determination of the b-hadrons must be studied. The lepton information is not included in the training of the neural network to obtain

the charge of the b-quark. However, a small correlation of $\rho_{bl} = 1.036 \pm 0.005$ is found, where ρ_{bl} is the ratio of efficiencies to correctly find the charge of b-quark in a hemisphere which contains a lepton over all hemispheres. This is used to reweight the Monte Carlo events, and twice the statistical uncertainties on ρ_{bl} is used to obtain systematic uncertainties.

A more critical bias exists between the neural network output and the b-hadron composition. The neural network output for a hemisphere containing a charged b-hadron is more likely to give the correct charge of the b-quark than a hemisphere containing a neutral b-hadron. The effect of this bias is to increase the number of incorrectly determined charge of the b-quark for neutral b-hadrons. However, artificially adjusting the simulation to account for this bias results in very little change in the measured branching fractions. A more critical approach is to compare the measured branching fractions with the ones obtained without the charge correlation. By combining the two classes of leptons into one, the lepton spectrum contains the contributions from the direct decay and both modes of the secondary decays. The fit of the three modes is performed by alternatively fixing one rate of the two secondary decays modes, starting with the rate of $b \to \bar{c} \to \ell$ fixed to the result of the analysis, until the fit converges. Figure 5.4 shows the distributions of the three modes as a result of the fit. The difference between the branching ratios obtained in this fit and the ones obtained with the charge correlation is used as a systematic uncertainty. The contributions to the systematic uncertainties of the correlation studies are listed in Table 5.4.

Table 5.4 Uncertainties from correlation studies

Source	ΔBR $\times 10^{-2}$		
	$b \to \ell$	$b \to \bar{c} \to \ell$	$b \to c \to \ell$
ℓ-charge tag correlation	∓ 0.08	∓ 0.03	∓ 0.09
b-hadron composition	∓ 0.08	∓ 0.15	∓ 0.11

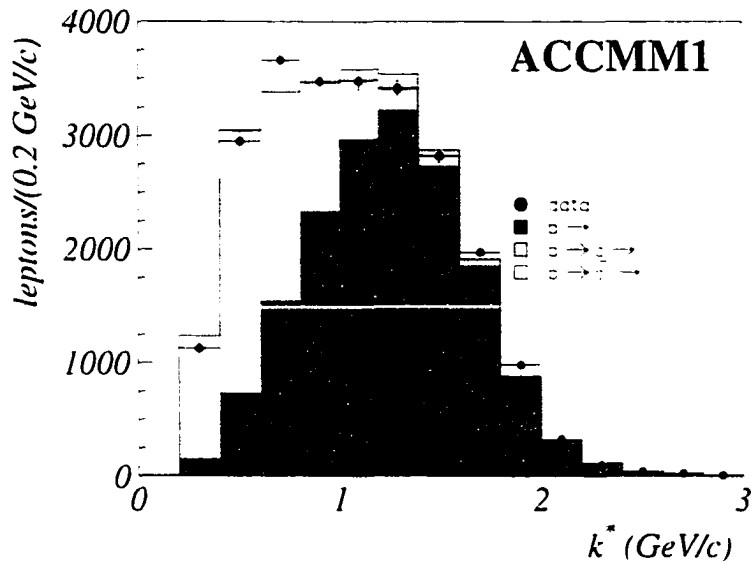

Figure 5.4 Results of fitting the lepton spectrum without the charge correlation.

5.3.1.2 Treatment of leptons

To match the efficiencies of selecting leptons in the real and simulated data, corrections are applied to the simulated leptons, as discussed in Section 4.3.3. The probabilities of selecting hadrons as leptons are also matched between the two sets of data. These corrections contain uncertainties in the measurement from both statistical and systematic sources. To study the effects of the uncertainties, the correctional factors listed in Table 4.5 are varied to the extremes of the uncertainties. In addition, the residual contamination in the electron sample by the converted photons are varied by 10%. The resulting changes in the measurements of branching fractions are listed in Table 5.5.

Table 5.5 Uncertainties resulting from lepton treatment

		$\Delta BR \times 10^{-2}$		
Source	Range	$b \to \ell$	$b \to \bar{c} \to \ell$	$b \to c \to \ell$
ϵ_e	±3%	∓0.18	∓0.04	∓0.15
ϵ_μ	±2.8%	∓0.13	∓0.05	∓0.10
Misidentified e	±8%	±0.01	∓0.11	∓0.08
Misidentified μ	±6.5%	±0.01	∓0.08	∓0.05
Converted γ	±10%	±0.01	∓0.04	∓0.03

5.3.1.3 *b*-tagging and related bias

While selecting b-hemispheres, there are two items that may influence the measurements. The first is in the calculation of the purity in the selected hemispheres. In the calculation of the b-tagging purity, the efficiencies in tagging c- and uds-quarks are estimated from the simulation. These efficiencies, ε_c and ε_{uds}, are varied up to 9% and 22% of the estimated values, respectively, following the results of the b-tagging studies [24]. In addition, the values of R_b and R_c are varied to reflect the measured uncertainties to study the effects.

The second influence comes from a more discrete source. In tagging b-hemispheres, a correlation between the b-tagging and the selection of leptons in the opposite hemisphere exists. As the acceptance requirements for the leptons cause the correlation, electrons and muons exhibit different correlations. The ratio, ρ, of the fraction of selected leptons in the opposite hemisphere to b-tagged one to the fraction of selected leptons in unbiased hemisphere is found for each lepton:

$$\rho_{electron} = 1.057 \pm 0.005$$

$$\rho_{muon} = 1.041 \pm 0.005,$$

where the uncertainties are statistical. Twice the uncertainties in the above ratios are used to study the effects of this correlation. The contributions of these b-tagging related items to the overall measurements are listed in Table 5.6.

Table 5.6 Uncertainties resulting from b-tagging procedure

Source	Range	ΔBR $\times 10^{-2}$ $b \to \ell$	$b \to \bar{c} \to \ell$	$b \to c \to \ell$
ε_c	$\pm 9\%$	<0.01	∓ 0.01	∓ 0.01
ε_{uds}	$\pm 22\%$	<0.01	± 0.01	∓ 0.01
R_b	0.2170 ± 0.0009	<0.01	<0.01	<0.01
R_c	0.1734 ± 0.0048	<0.01	<0.01	<0.01
$\hat{\epsilon}$ vs b-tag correlation	$\pm 1\%$	∓ 0.09	∓ 0.03	∓ 0.09

5.3.1.4 Fitting procedure

In the fitting procedure, the simulation spectra for different decay modes are assumed to be made up from infinite statistics. However, since no such sample is possible, the existence of statistical uncertainties in the simulation spectra needs to be taken into account. The fitting procedure is repeated including the statistical uncertainties in the simulation spectra. The difference between the branching fractions while including and excluding the statistical uncertainties is listed in Table 5.7.

5.3.2 Theoretical uncertainties

A uniform treatment of the theoretical uncertainties is proposed by the LEPEWWG to ensure consistency in reporting the measurements by different LEP experiments [25]. This includes the uncertainties in the assumed branching fractions of the background processes, the dependency on decay models and the fragmentation model for b- and c- hadrons. The uncertainties resulting from the choice of the leptonic decay models are reported separately from others.

Table 5.7 Uncertainties in fitting with finite simulation sample

Source	ΔBR $\times 10^{-2}$ $b \to \ell$	$b \to \bar{c} \to \ell$	$b \to c \to \ell$
MC statistics	∓ 0.03	∓ 0.01	∓ 0.03

5.3.2.1 Fragmentation functions

The amount of available energy for the b-hadrons after the fragmentation process follows a phenomenological model in the simulation, as this quantity cannot be calculated from QCD. The adapted model for the heavy quarks in this analysis is that of Peterson *et al.* [29]. In this model, the heavy quarks, with their large masses, are assumed to be less influenced by the fragmentation process. The transferred energy to the hadrons can be described by the longitudinal fragmentation function:

$$f(z) \sim \frac{1}{z[1 - 1/z - \epsilon_q/(1-z)]^2}, \tag{5.1}$$

where z is the fraction of the initial quark energy:

$$z = \frac{(E + p_L)_{hadron}}{(E + p_L)_q}. \tag{5.2}$$

Figure 5.5 shows the fragmentation functions for different quarks. The current measurement of the mean fractional energy of the b-quarks, $x_E(b)$, is $(70.2 \pm 0.8)\%$ of the initial quark energy. This value is varied according to its statistical uncertainty to obtain the contribution. The same procedure is repeated with the mean fractional energy of c-quarks of $x_E(c) = (48.4 \pm 0.8)\%$. The results are shown in Table 5.9.

5.3.2.2 Assumed branching fractions

In studying the effects of the branching fractions of the individual upper–vertex leptonic modes described in Section 4.3.4, the c-baryon mode, $b \to W \to \Lambda_c \to \ell$, is

Table 5.8 Uncertainties in the choice of fragmentation model

		ΔBR $\times 10^{-2}$		
Source	Range	$b \to \ell$	$b \to \bar{c} \to \ell$	$b \to c \to \ell$
$x_E(b)$	0.702 ± 0.008	∓ 0.03	± 0.05	∓ 0.07
$x_E(c)$	0.484 ± 0.008	∓ 0.01	± 0.01	∓ 0.01

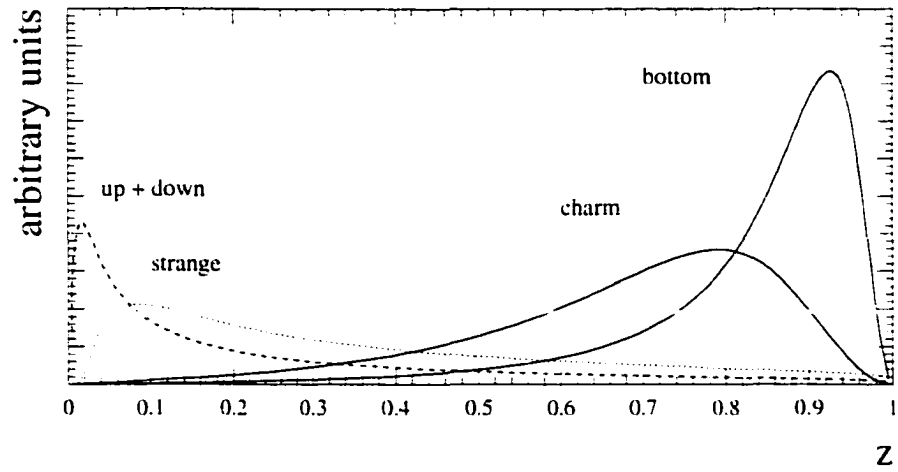

Figure 5.5 Fragmentation functions for different quarks. Peterson fragmentation function is used for heavy quarks with $\epsilon_b = 0.006$ and $\epsilon_c = 0.06$ in the graph.

neglected in consideration for its relatively small contribution to the overall branching fraction. However, the difference between the branching fractions for the other two modes, via $D^{0/+}$ and D_s, leads to the change in shape of the momentum spectrum for the upper–vertex leptons. The difference in the spectrum for the extremes of the allowed bounds in the branching fractions is shown in Figure 5.6 and is used to study the effects to the measurements.

For the background events, which are subtracted before the fitting procedure, the uncertainties in the measured branching fractions for the processes, $b \to \tau \to \ell$, $b \to J/\Psi \to \ell$ and $c \to \ell$ are taken into account [25]. The resulting contribution from the uncertainties in the branching fractions of these processes is listed in Table 5.9.

5.3.2.3 Decay models

The presentation of the branching fraction for the $b \to \ell$ process follows the prescription of the LEPEWWG. The central value of the measurement is obtained by using the ACCMM model. The upper and the lower bounds of the uncertainties from

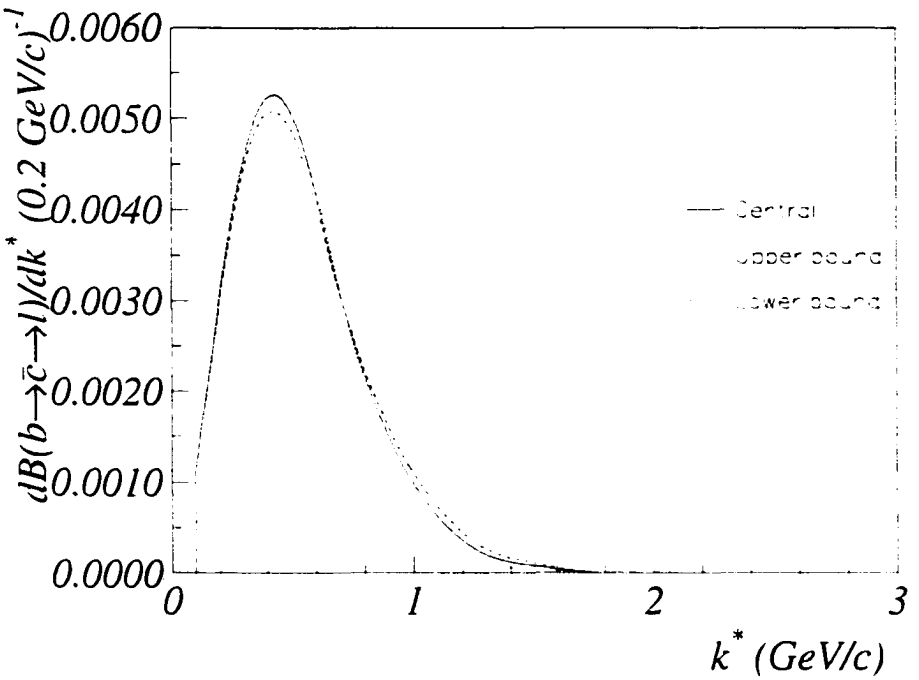

Figure 5.6 The upper–vertex lepton spectrum. The solid curve is the central value, and the other curves represent the extremes of the bounds in the branching fractions

Table 5.9 Uncertainties from the assumed branching fractions

Source	Range	ΔBR $\times 10^{-2}$ $b \to \ell$	$b \to \bar{c} \to \ell$	$b \to c \to \ell$
$\frac{b\to W\to D}{b\to W\to D_s}$	$(1.28^{+1.52}_{-0.61})$	$^{+0.04}_{-0.04}$	$^{-0.09}_{+0.08}$	$^{+0.03}_{-0.03}$
BR($b \to \tau \to \ell$)	$(0.452 \pm 0.074)\%$	∓ 0.02	∓ 0.07	< 0.01
BR($b \to J/\Psi \to \ell$)	$(0.07 \pm 0.02)\%$	∓ 0.06	± 0.03	∓ 0.01
BR($c \to \ell$)	$(9.8 \pm 0.5)\%$	∓ 0.03	∓ 0.13	∓ 0.05

the use of different decay models are obtained by using ISGW and ISGW** in that respective order. For the process of $b \to c \to \ell$, the ACCMM1 model is used to obtain the central value. The ACCMM2 and the ACCMM3 models are used to provide the upper and the lower bounds. These uncertainties from the use of different decay models are summarized in Table 5.10

5.4 Summary of results

Combining the uncertainties in both experimental methods and modelling, excluding those of decay models, the total systematic uncertainties are shown in Table 5.11. These uncertainties, along with the ones from the use of different semileptonic decay models, are put together with the fitting results to give the following measurements:

$$\begin{aligned}
\mathrm{BR}(b \to \ell)(\%) &= 10.75 \pm 0.15(\mathrm{stat}) \pm 0.28(\mathrm{syst})^{-0.24}_{+0.43}(\mathrm{model}) \\
\mathrm{BR}(b \to c \to \ell)(\%) &= 7.99 \pm 0.27(\mathrm{stat}) \pm 0.28(\mathrm{syst})^{-0.21}_{-0.10}(\mathrm{model}) \\
\mathrm{BR}(b \to \bar{c} \to \ell)(\%) &= 1.34 \pm 0.30(\mathrm{stat}) \pm 0.29(\mathrm{syst})^{-0.36}_{-0.58}(\mathrm{model}).
\end{aligned}$$

The measurements obtained in the analysis are within the bounds of expectation. For the upper–vertex leptons, as the first measurement of its value, the branching fraction is within the expected bounds discussed in Section 4.3.4 and, therefore, does support the preliminary measurements of the branching fractions for the upper–

Table 5.10 Uncertainties resulting from the dependency of decay models

Source	Range	$\Delta\mathrm{BR} \times 10^{-2}$		
		$b \to \ell$	$b \to \bar{c} \to \ell$	$b \to c \to \ell$
$b \to \ell$ model	ACCMM $(^{+ISGW}_{-ISGW**})$	$^{-0.23}_{+0.42}$	$^{+0.36}_{-0.58}$	$^{+0.04}_{-0.04}$
$c \to \ell$ model	ACCMM1 $(^{+ACCMM2}_{-ACCMM3})$	$^{-0.07}_{+0.07}$	$^{+0.06}_{-0.05}$	$^{-0.21}_{+0.09}$
Total Models		$^{-0.24}_{+0.43}$	$^{+0.36}_{-0.58}$	$^{-0.21}_{+0.10}$

Table 5.11 Combined systematic uncertainties

decay mode	uncertainties in BR $\times 10^{-2}$
$b \to \ell$	± 0.28
$b \to \bar{c} \to \ell$	± 0.29
$b \to c \to \ell$	± 0.28

vertex D mesons by CLEO and ALEPH. This may be yet another clue to the enhancement of the upper vertex, which should result in an increase of the charm count.

6 CONCLUSION

The baffling discrepancy between the theoretical prediction and the measurement of the inclusive b-hadron semileptonic branching fraction at the lower energy experiments inspired a series of new calculations. Added to this possible discrepancy was the disagreement among the experimental measurements conducted at higher and lower energy facilities, namely at LEP and CLEO. Although the earlier measurements of the LEP experiments were inside the theoretical bounds, some questionable measuring techniques led to a call for a new set of analyses. The performance of b-tagging algorithm and particle identification has improved substantially in the recent years. Taking advantage of such improvements, better designed analyses were developed to provide more precise measurements.

One such analysis was presented in this thesis. By recognizing the difficulty of fitting different decay modes, some of whose momentum spectra were similar and therefore difficult to distinguish, a scheme was developed to separate as much as possible different decay modes before the fitting procedure. The charge correlation technique effectively separated $b \to \ell$ and $b \to c \to \ell$ decay modes. The fitting process was further eased by performing the fit to the lepton momentum in the b-hadron rest frame, as opposed to the traditional fit to the transverse momentum spectrum. In addition, the first reported measurement of the branching fraction for the $b \to \bar{c} \to \ell$ process was a natural outcome of this technique.

Interestingly, the final results from this analysis alone do not demonstrate a discrepancy from the theoretical expectation, since they are consistent with the theory

for certain values of the charm count. The enhancement of the upper–vertex mode, $b \to \bar{c} \to \ell$, as preliminarily indicated by CLEO and ALEPH, was evident. This situation now begs for a new round of updated measurements of the charm count. In the following section, three other analyses conducted by the DELPHI experiment to measure the semileptonic branching fraction are summarized. The details of all the analyses can be found in [8]. Then a few concluding remarks follow.

6.1 Summary of DELPHI results

The DELPHI experiment initiated four independent analyses of the semileptonic branching fraction. One group used a traditional method of single lepton and di-lepton spectra fit. In the single lepton fit, leptons were selected in the opposite hemisphere to the b-tagged hemisphere, and the transverse momentum spectrum of the leptons was fitted with the expected spectra of $b \to \ell$, $b \to c \to \ell$, $b \to \bar{c} \to \ell$, other b products and non-b products. For the di-lepton fit, instead of tagging b hemispheres, energetic leptons were selected to tag one hemisphere, and other leptons were searched for in the opposite hemisphere. By correlating the charges of the energetic lepton and of the opposite leptons, the B^0 mixing angle could be measured along with the semileptonic branching fraction. In combining the single and di-lepton fit to the transverse momentum spectra, the obtained result was

$$\mathcal{B}_{\mathrm{SL}}(\%) = 10.75 \pm 0.11(\mathrm{stat}) \pm 0.26(\mathrm{syst})^{-0.25}_{+0.42}(\mathrm{model}) \tag{6.1}$$

averaged over electrons and muons in the 1994 and 1995 data–taking periods.

The approach of another group, as in the case of the analysis presented here, was to take advantage of the better separation power among the different decay modes by fitting the expected spectra to the lepton momentum spectrum in the b-hadron rest frame rather than to the transverse momentum spectrum. The jet charge was found

in the b-tagged hemisphere and was associated with the charge of the leptons found in the opposite hemisphere. Two quantities

$$\begin{aligned} \lambda_Q &= (\text{jet charge in the } b\text{-tagged hemisphere}) \\ &\quad \times (\text{charge of lepton in the opposite hemisphere}) \\ k^* &= \text{lepton momentum in } b\text{-hadron rest frame} \end{aligned}$$

were fitted with expected spectra for $b \to \ell$, $b \to c \to \ell$ and $b \to \bar{c} \to \ell$ to give

$$\mathcal{B}_{\mathrm{SL}}(\%) = 10.78 \pm 0.14(\mathrm{stat}) \pm 0.29(\mathrm{syst})^{-0.34}_{+0.53}(\mathrm{model}). \tag{6.2}$$

The third group utilized all hadronic events and separated the quark flavors by employing a multi-variate method. Then for each quark flavor, the momentum and transverse momentum spectra of muons were fitted with $b \to \ell$, $b \to c \to \ell$ and background. This study covered the data taken from 1992 to 1995, and only the muons were considered in the measurement. The branching fraction was determined to be

$$\mathcal{B}_{\mathrm{SL}}(\%) = 10.69 \pm 0.11(\mathrm{stat}) \pm 0.28(\mathrm{syst})^{-0.37}_{+0.44}(\mathrm{model}). \tag{6.3}$$

The results from these three analyses and the ones presented in this thesis were combined to give a new DELPHI average of

$$\mathcal{B}_{\mathrm{SL}}(\%) = 10.73 \pm 0.08(\mathrm{stat}) \pm 0.22(\mathrm{syst})^{-0.30}_{+0.44}(\mathrm{model}), \tag{6.4}$$

taking into account the correlations among the measurements. This measurement is compatible with the updated measurements from other LEP experiments. Other averaged quantities are the branching fractions for cascade and upper–vertex leptons:

$$\mathrm{BR}(b \to c \to \ell)(\%) = 7.91 \pm 0.20(\mathrm{stat}) \pm 0.29(\mathrm{syst})^{+0.14}_{-0.20}(\mathrm{model}) \tag{6.5}$$

$$\mathrm{BR}(b \to \bar{c} \to \ell)(\%) = 1.69 \pm 0.18(\mathrm{stat}) \pm 0.26(\mathrm{syst})^{+0.30}_{-0.44}(\mathrm{model}). \tag{6.6}$$

Figure 6.1 shows the result of this analysis and the new DELPHI average in comparison to the theoretical bounds.

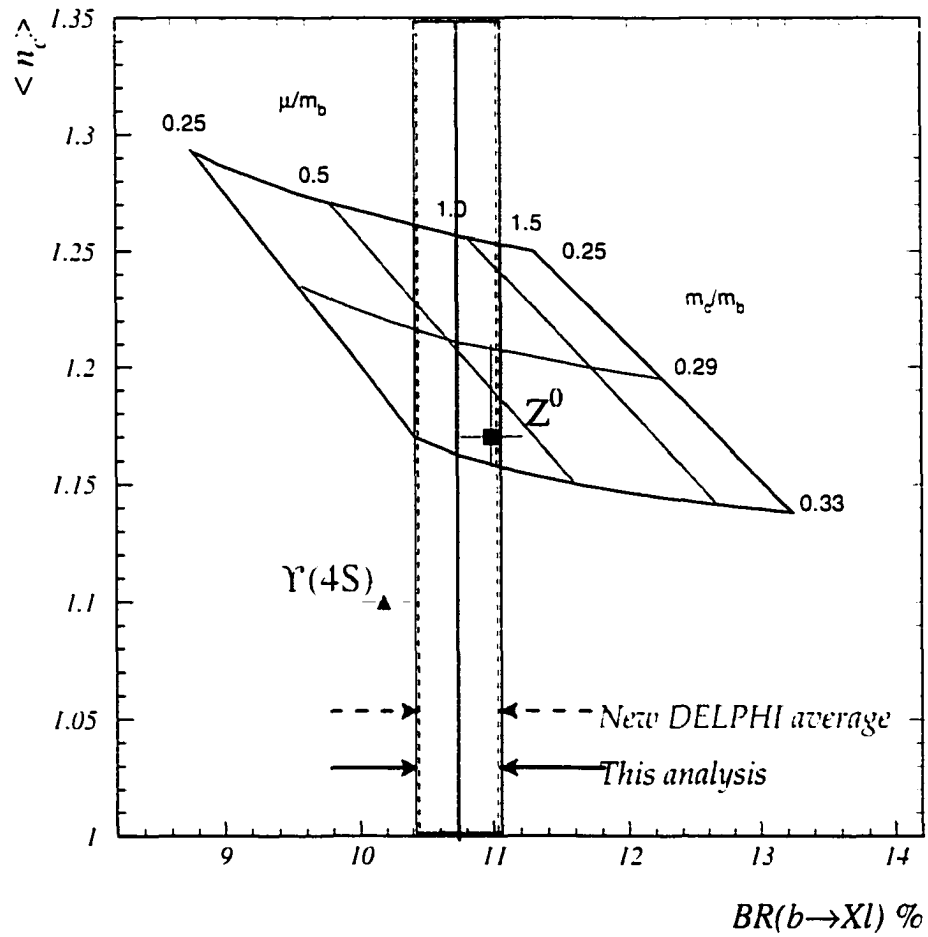

Figure 6.1 Bounds of measured $\mathcal{B}_{SL}$ shown with the theoretical boundary. The solid line represents the bounds of the measurement presented in the thesis, while the dashed line represents the bounds of DELPHI average.

6.2 Concluding remarks

The results of this study and those of other analyses at DELPHI do not indicate a disagreement between the measured and the theoretical values of $\mathcal{B}_{SL}$. To understand the difference in the measurements among different facilities, analyses conducted at lower energy facilities need to be examined and compared to the analyses conducted at LEP. The measurement of a recent CLEO analysis is widely quoted as a model-independent measurement and is used as the CLEO result [6]. In its analysis, similar to the di-lepton analysis at DELPHI, a high-momentum lepton is used to tag one B and the lepton from the other B is search for. By correlating the charges of the two leptons, direct leptons can be separated from the secondary leptons. The mixing of neutral B is unfolded in each momentum bin using the CLEO average for the mixing parameter. A model is used to extrapolate only the low momentum portion of the direct lepton spectrum. The result obtained is

$$\mathrm{BR}(B \to X\ell) = (10.49 \pm 0.17(\mathrm{stat.}) \pm 0.43(\mathrm{syst.}))\%, \tag{6.7}$$

and the lepton spectra are shown in Figure 6.2. The influence of the upper–vertex leptons is considered negligible.

The measurement of CLEO is combined with those of other $\Upsilon(4S)$ experiments to provide the average of $(10.45 \pm 0.21)\%$ [18]. To compare this measurement at lower energy facilities to the results obtained by DELPHI, a correction factor is applied, assuming the same semileptonic width for all b-hadrons:

$$BR^{b}_{SL} = \frac{\tau_b}{\tau_B} BR^{B}_{SL}, \tag{6.8}$$

where the superscript B represents B mesons, and b represents b-hadrons. With $\frac{\tau_b}{\tau_B} = 0.974$ [18], the two measurements are just over one standard deviation apart. The disagreement at this level may be warranted. While the average for the $\Upsilon(4S)$

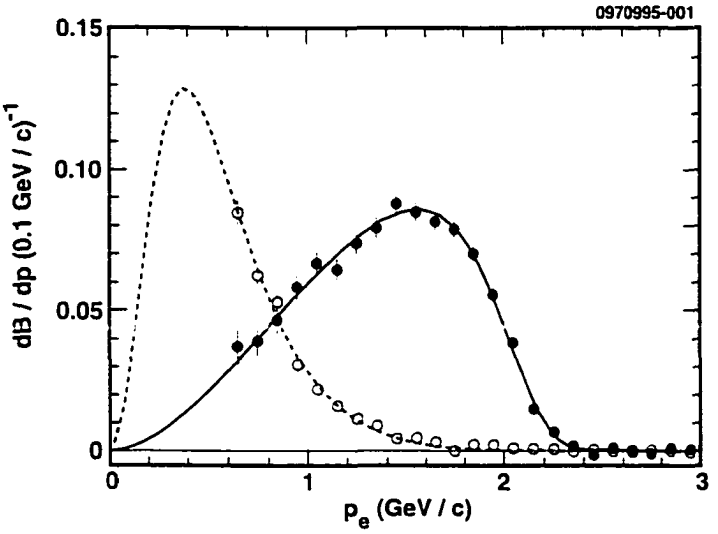

Figure 6.2 Spectra for direct leptons in black circles and cascade leptons in open circles by the CLEO collaboration. Adapted from [6].

experiments includes the results of older analyses, the results of more recent analyses, such as the one presented above, are consistent with those of LEP experiments within errors. To compare the two measurements in a fair setting, future analyses at LEP need to reduce the dependency on decay models, which contribute the most to the overall uncertainties. With $\mathcal{B}_{SL}$ seemingly under control, the answer to the question of whether any discrepancies exist between the theoretical prediction and the experimental measurements needs to come from the more precise and updated measurement of n_c. Only then, words such as baffling can be used to describe the problem in the $\mathcal{B}_{SL}$ and n_c plane. Until such time comes, however, I borrow the words of one physicist to best describe the current situation [16]:

> In a few years from now, many ... will be known, ... discovered and ... observed. Then we will probably laugh about the few 2 sigma discrepancies that we have to deal with now.

REFERENCES

[1] I. Bigi, B. Blok, M. Shifman, A. Vainshtein, *The Baffling Semileptonic Branching Ratio of B Mesons*, Phys. Lett. **B323**, (1994) 408.

[2] ALEPH Collaboration, D. Buskulic *et al.*, Z. Phys. **C62**, (1994) 179.

[3] DELPHI Collaboration, P. Abreu *et al.*, Z. Phys. **C66**, (1995) 323.

[4] L3 Collaboration, B. Adeva *et al.*, Phys. Lett. **B261**, (1991) 117.

[5] OPAL Collaboration, R. Akers *et al.*, Z. Phys. **C60**, (1993) 199.

[6] CLEO Collaboration, B. Barish *et al.*, Phys. Rev. Lett. **76**, (1996) 1570.

[7] Argus Collaboration, H. Albrecht *et al.*, Phys. Lett. **B318**, (1993) 397.

[8] DELPHI Collaboration, P. Abreu *et al.*, *Measurement of the semileptonic b branching fractions and average b mixing parameter in Z decays*, submitted to E. Phys. J.

[9] L3 Collaboration, M. Acciarri *et al.*, E. Phys. J. **C13**, (2000) 47.

[10] OPAL Collaboration, G. Abbiendi *et al.*, E. Phys. J. **C13**, (2000) 225.

[11] N. Cabibbo, L. Maiani, Phys. Lett. **B79**, (1978) 109.

[12] G. Altarelli, S. Petrarca, Phys. Lett. **B261**, (1991) 303.

[13] E. Bagan, P. Ball, V. Braun, P. Gosdzinsky, *Theoretical Update of the Semileptonic Branching ratio of B Mesons*, Phys. Lett. **B342**, (1995) 362;
Erratum, Phys. Lett. **B374**, (1996) 363.

[14] G. Buchalla, I. Dunietz, H. Yamamoto, *Hadronization of $b \to c\bar{c}s$*, Phys. Lett. **B364**, (1995) 188.

[15] A. Kagan, *Implications of TeV Flavor Physics for the $\Delta I = 1/2$ Rule and $BR_\ell(B)$*, SLAC-PUB-6626, hep-ph/9409215.

[16] M. Feindt, *B Physics*, IEKP-KA/98-4.

[17] N. Isgur *et al.*, *Semileptonic B and D decays in the quark model*, Phys. Rev. **D39** (1989) 799.

[18] Particle Data Group Eur Phys. J. **C3** (1998) 1.

[19] DELPHI Collaboration, P. Aarnio *et al.*, Nucl. Inst. Meth. **A303** (1991) 233; DELPHI Collaboration, P. Abreu *et al.*, Nucl. Inst. Meth. **A378** (1996) 57.

[20] Z. Albrecht, M. Feindt, M. Moch, *High efficiency - high purity hadron identification for* DELPHI,
DELPHI note 99-150 RICH 95.

[21] C.Kreuter, *Electron Identification using a Neural Network*,
DELPHI note 96-169 PHYS 658.

[22] CN/ASD Group, *ZEBRA User's Guide*, Program Library Q100, CERN, 1993.

[23] JADE Collaboration, W.Bartel *et al.*, Z. Phys. **C33** (1983) 23; S.Bethke et al., Phys. Lett. **B213** (1988) 235.

[24] DELPHI Collaboration, P. Abreu *et al.*, *A precise measurement of the partial decay width ratio $R_b^0 = \Gamma_{b\bar{b}}/\Gamma_{had}$*, E. Phys. J. **C10** (1999) 415.

[25] The LEP Electroweak Working Group
Input Parameters for the LEP/SLD Electroweak Heavy FlavorResults, LEPHF/98-01, July, 1998.

[26] L. Lönnblad *et al.*, *Pattern Recognition in High Energy Physics with Artificial Neural Networks – JETNET*, Computer Physics Communications, **70** (1992) 167.

[27] Z. Albrecht *et al.*, *BSAURUS - A package for inclusive B-reconstruction for* DELPHI *data*, DELPHI note 2000-069 PHYS 868.

[28] T. Sjöstrand CERN-TH/7112/93 (1993), revised August 1995; Comp. Phys. Comm. **82** (1994) 74.

[29] C.Peterson *et al.*, Phys.Rev. **D27** (1983) 105.

ACKNOWLEDGMENTS

It was two o'clock in the morning at the DELPHI control room. I was sitting on an ergonomic chair with four different computer monitors telling me that everything was okay with DELPHI. An older gentleman was entertaining me with the stories of the first chaotic days of DELPHI when taking a shift meant actual work, both mentally and physically. Indeed, things have come a long way. The work of over 550 physicists from 56 universities and laboratories from all over the world has produced a great supporting environment, in which a clueless graduate student can learn and turn out a decent analysis with relative ease. It is in this spirit that I am indebted to all DELPHI members, past and present.

This analysis, as with many others, is a patch work of many components. The most important component is the *b*-hadron reconstruction and the related neural networks, which Michael Feindt and his army at Karlsruhe have done an incredible job. Another important component is the study of lepton efficiencies and misidentification. Martino Margoni, Franco Simonneto and Pierre Antilogus have each withstood endless criticism in standardizing the treatment of leptons, thereby making my life and those of other groups simpler and easier. Much of my shortcomings in this analysis were compensated by the great quality control of the b,c-semileptonic team. Marta Calvi in particular deserves much credit in the success of this analysis and for leading the effort to publish the results from all the groups.

Living on a foreign land did not prove to be an easy task. However, the help and the kind words of Jim Grahl and Alex Firestone provided much needed relief.

In joining the DELPHI community, I have benefited greatly from the generosity of Michael Feindt. His single-handed enthusiasm for physics and willingness to guide me throughout my stay at CERN and beyond have resulted in my renewed appreciation of physics. I also thank the kind people at Karlsruhe: Gary, Zoltan, Marcus and Christian in particular, for their hospitality during my short stay. I am privileged to have worked with them.

All this would not have been possible without the generous support of my advisor, Eli Rosenberg. His patience and guidance in this long journey has been most valuable. My gratitude also goes to Linda Shuck for all her generosity. To close, I am forever indebted to my dear Sandy for her support and companionship through all the difficult times and to my parents, to whom this thesis is dedicated, for their support and letting me "repair" every single radio in the house just to satisfy a child's curiosity.

This work was performed under the Department of Energy grant number DE-FG02-94ER40817.